Target Detection With Imperfect Waveform Separation in Distributed MIMO Radar

Pu Wang, *Senior Member, IEEE*, and Hongbin Li, *Fellow, IEEE*

***Abstract*—This paper considers target detection in distributed multiple-input multiple-output (MIMO) radar with imperfect waveform separation at local receivers. The problem is formulated as a binary composite hypothesis testing problem, where target residuals due to imperfect waveform separation are explicitly modeled as a subspace component in the alternative hypothesis, while disturbances including the clutter and thermal noise are present under both hypotheses. Under assumptions of *fluctuating* and *non-fluctuating* target amplitude over a scan, e.g., Swerling models, we particularly consider a distributed hybrid-order Gaussian (DHOG) signal model and develop the generalized likelihood ratio test (GLRT) which relies on the maximum likelihood (ML) estimation of the target amplitude and the residual covariance matrix under the alternative hypothesis. The Cramér-Rao bounds (CRBs) on estimating the target amplitude and residual subspace covariance matrix are derived. Simulation results in both local and distributed scenarios confirm the effectiveness of the proposed GLRT and show improved performance in terms of receiver operating characteristic (ROC) by exploiting the existence of target residual component.**

***Index Terms*—Moving target detection, distributed MIMO radar, hypothesis test, subspace model, generalized likelihood ratio test, maximum likelihood estimation, Cramér-Rao bound.**

I. Introduction

In RECENT years, target detection using orthogonal MIMO waveforms have received significant interest. In this work, we focus on target detection using distributed MIMO radar, which employ widely separated antennas to form the transmit and, respectively, receive aperture, and probe a scene using multiple orthogonal waveforms. The distributed MIMO detection allows one to exploit the spatial or geometric diversity to enhance target detection, since targets often exhibit significant azimuth-selective backscattering with tens of dB of fluctuation in their radar cross section (RCS) [1]–[4]. The effect of clutter was also studied in [3], [5]–[7] for moving target detection. Other related efforts have been placed to waveform design [8]–[13], synchronization effect [14]–[16], exploitation of target sparsity in the spatial and/or Doppler domains [17], [18], impact of nonhomogeneous interference and registration errors [19]–[21], optimal transmit power allocation and antenna configuration [22]–[25], exploitation of prior knowledge [26]–[28], deployment on moving platforms [29] and cooperative radar-communication platforms [30]–[32].

These studies usually assume the multiple transmitters transmit orthogonal probing waveforms with zero cross-correlation, and these transmit waveforms are perfectly separated at each receiver by matched filter processing. However, such ideal waveform separation is impossible across all Doppler frequencies and time delays [33], [34]. Therefore, the effect of waveform residuals has to be considered in the target detection for distributed MIMO radars. Particularly, [34] and [35] investigated the sensitivity or robustness of distributed MIMO detectors under the condition of imperfect waveform separation. In the following, we provide a mathematical model explicitly accounting for target residuals due to imperfect waveform separation. It is interesting to see that, the target residuals only appear when the target of interest is present, i.e., in the alternative hypothesis, and the residual content shows a subspace structure spanned by Fourier bases of bistatic Doppler frequencies over different transmitter-receiver (Tx-Rx) pairs.

In this paper, we take into account the existence of such target residuals in the baseband receiving signal and formulate the target detection as a binary composite hypothesis testing problem where the alternative and null hypotheses differ from not only the target signal but also the target residual. We consider several standard models on the target amplitude over a scan, *fluctuating*, *non-fluctuating* or both, and propose a distributed hybrid-order Gaussian (DHOG) model. Under the DHOG model, we derive the *exact* ML estimation under the alternative hypothesis and the *exact* GLRT. It is found that the exact ML estimation yields closed-form solutions in certain circumstances depending on the geometry of terms related to the received signal, target steering vector, residual subspace matrix, and disturbance covariance matrix, and requires a numerical optimization of a monotonically increasing function over a confined region. The Fisher information matrix (FIM) associated with the parameter estimation problem is also derived and utilized to find the Cramér-Rao bounds (CRBs) on unknown parameter estimation under the alternative hypothesis. Simulation results in both local and distributed scenarios confirm the effectiveness of the proposed GLRT and show much improved performance in terms

Manuscript received May 7, 2019; revised August 12, 2019, September 24, 2019, and December 13, 2019; accepted December 14, 2019. Date of publication January 6, 2020; date of current version February 14, 2020. The associate editor coordinating the review of this manuscript and approving it for publication was Dr. Aboulnasr Hassanien. The work of H. Li was supported in part by the National Science Foundation under Grants ECCS-1609393 and ECCS-1923739. This article was presented in part at the IEEE Radar Conference, Adelaide, SA, Australia, September 2003. *(Corresponding author: Pu Wang.)*

P. Wang is with the Mitsubishi Electric Research Laboratories (MERL), Cambridge, MA 02139 USA (e-mail: pwang@merl.com).

H. Li is with the Department of Electrical and Computer Engineering, Stevens Institute of Technology, Hoboken, NJ 07030 USA (e-mail: hongbin.li@stevens.edu).

Digital Object Identifier 10.1109/TSP.2020.2964227

1053-587X © 2020 IEEE. Personal use is permitted, but republication/redistribution requires IEEE permission.
See https://www.ieee.org/publications/rights/index.html for more information.

Authorized licensed use limited to: Stevens Institute of Technology. Downloaded on August 18,2020 at 19:27:31 UTC from IEEE Xplore. Restrictions apply.

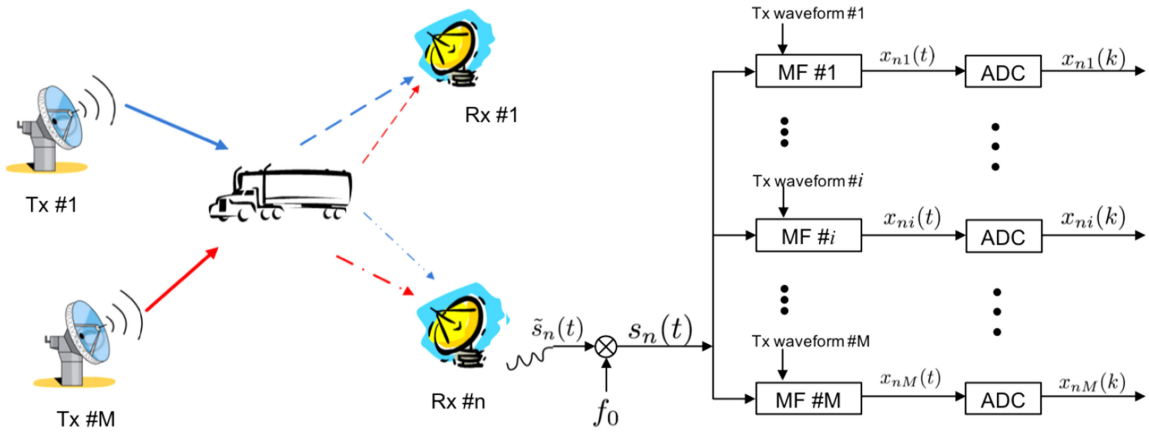

Fig. 1. Moving target detection of distributed MIMO radar and baseband signal at local receivers.

of receiver operating characteristic (ROC) by exploiting the existence of target residual component.

The remainder of the paper is organized as follows. The signal model is introduced in Section II. In Section III, we present the distributed MIMO detection problem with three formulations of the target residuals: 1) distributed first-order Gaussian model (DFOG); 2) distributed second-order Gaussian model (DSOG); and 3) a new distributed hybrid-order (first-order and second-order) Gaussian model. Section IV proposes the GLRT solution to the DHOG formulation with exact ML estimation for the target amplitude and the residual covariance matrix. Simulation results are provided in Section V. Finally, conclusions are drawn in Section VI.

II. Signal Model: Accounting for Target Residual From Imperfect Waveform Separation

Consider a distributed MIMO system with M transmit sites (Tx) and N receive sites (Rx) in Fig. 1. We assume that the distributed MIMO system probes a common area of interest using M orthogonal waveforms from M transmit antennas. Pulsed transmission is employed as in standard Doppler radars. Each transmitter sends a succession of K periodic pulses, i.e., K repetitions of an orthogonal waveform, over a coherent processing interval (CPI). Specifically, at the m-th transmit site, the transmitted burst of pulses are given as

$$\tilde{s}_m(t) = \beta_m u_m(t) e^{j(2\pi f_0 t + \psi_m)}, \tag{1}$$

where

$$u_m(t) = \sum_{k=0}^{K-1} u_{pm}(t - kT_{\text{PRI}}), \tag{2}$$

is the baseband transmitted signal, $u_{pm}(t)$ is the complex envelope of a single pulse, β_m is the transmit amplitude at the m-th transmitter, f_0 is the carrier frequency, and ψ_m is the initial phase. The pulse waveform $u_{pm}(t)$ is of duration T_p and has unit energy. Assuming a moving target at a distance R_m to the m-th transmitter and a distance R_n to the n-th receiver with a speed of $\mathbf{v} = [v_x, v_y]^T$, the observed signal $\tilde{s}_n(t)$ (see Fig. 1) at the n-th receiver consists of echoes from a moving target illuminated by M orthogonal transmitting waveforms [3]

$$\tilde{s}_n(t) = \sum_{m=0}^{M-1} \alpha_{nm} \xi_{nm} \beta_m u_m(t - \tau_{nm}) \times e^{j2\pi(f_0 + f_{nm})(t - \tau_{nm})} e^{j\psi_m}, \tag{3}$$

where α_{nm} accounts for the channel gain for the (m, n)-th Tx-Rx pair:

$$\alpha_{nm} = \sqrt{\frac{G_T^m G_R^n \lambda^2}{(4\pi)^3 R_m^2 R_n^2}}, \tag{4}$$

given the transmitting and receiving antenna gains G_T^m and G_R^m and the wavelength $\lambda = c/f_0$ with c denoting the waveform speed, ξ_{nm} is the target reflection amplitude for the (m, n)-th Tx-Rx pair, $\tau_{nm} = (R_m + R_n)/c$ is the delay for the (m, n)-th Tx-Rx pair, and

$$f_{nm} = \frac{T_{\text{PRI}}}{\lambda} \left[v_x(\cos\theta_{tm} + \cos\theta_{rn}) + v_y(\sin\theta_{tm} + \sin\theta_{rn}) \right] \tag{5}$$

is the normalized bistatic target Doppler frequency with $\theta_{t/r}$ denoting the transmitting/receiving angles with respect to the target. It is worth noting that, for a distributed MIMO radar with widely separated Tx-Rx pairs, it can observe both v_x and v_y due to multiple different projections of the velocity vector $\mathbf{v}$ into distinct observable bistatic velocities. For a mono-static radar, only the radial target velocity can be observed.

Equation (3) can be rewritten as

$$\tilde{s}_n(t) = \sum_{m=0}^{M-1} \tilde{\alpha}_{nm} u_m(t - \tau_{nm}) e^{j2\pi(f_0 + f_{nm})t} e^{-j2\pi f_0 \tau_{nm}} e^{j\psi_m} \tag{6}$$

where the equivalent target complex amplitude $\tilde{\alpha}_{nm} \triangleq \alpha_{nm} \xi_{nm} \beta_m e^{-j2\pi f_{nm} \tau_{nm}}$ absorbs all time-independent phase terms for the (m, n)-th Tx-Rx pair including the channel gain α_{nm}, target reflection amplitude ξ_{nm} and the phase term $e^{-j2\pi f_{nm} \tau_{nm}}$. After demodulation, the baseband signal at the

Authorized licensed use limited to: Stevens Institute of Technology. Downloaded on August 18,2020 at 19:27:31 UTC from IEEE Xplore. Restrictions apply.

n-th receiver is

$$s_n(t) = \sum_{m=0}^{M-1} \tilde{\alpha}_{nm} u_m(t-\tau_{nm}) e^{j2\pi f_{nm} t} e^{-j2\pi f_0 \tau_{nm}} e^{j\psi_m}. \tag{7}$$

A. Matched Filter Bank at Local Receivers

At the n-th receiver, a set of M matched filters as shown in Fig. 1, each matched with one of M orthogonal transmitting waveforms, are used to extract baseband signals corresponding to the (m,n)-th Tx-Rx pair. For the i-th matched filter at the n-th receiver, each pulse of $s_n(t)$ is matched separately with the receiver filter $h_i(t) = u_{pi}^*(-t)e^{-j\psi_i}$, where $u_{pi}(t)$ is the complex envelope of the i-th waveform in (2), $i = 0, \ldots, M-1$, and ψ_i denotes the phase mismatch due to synchronization errors at local matched filters. The output at the i-th matched filter is given as

$$\begin{aligned} x_{ni}(t) &= \int s_n(\nu) h_i(t-\nu) d\nu \\ &= \sum_{m=0}^{M-1} \tilde{\alpha}_{nm} e^{-j2\pi f_0 \tau_{nm}} e^{j(\psi_m - \psi_i)} \\ &\quad \times \sum_{k=0}^{K-1} \int_{\nu} u_{pm}(\nu - \tau_{nm} - kT_r) u_{pi}^*(\nu - t) e^{j2\pi f_{nm}\nu} d\nu \end{aligned} \tag{8}$$

By defining the cross ambiguity function (AF) as

$$\chi_{mi}(\tau, f) = \int_{\nu} u_{pm}(\nu) u_{pi}^*(\nu - \tau) e^{j2\pi f \nu} d\nu, \tag{9}$$

$x_{ni}(t)$ of (8) can be rewritten as

$$\begin{aligned} x_{ni}(t) &= \sum_{m=0}^{M-1} \tilde{\alpha}_{nm} e^{-j2\pi f_0 \tau_{nm}} e^{j(\psi_m - \psi_i)} \\ &\quad \times \sum_{k=0}^{K-1} \chi_{mi}(t - \tau_{nm} - kT_r, f_{nm}) e^{j2\pi k f_{nm} T_r}. \end{aligned} \tag{10}$$

The continuous signal of $x_{ni}(t)$ is then sampled by analog-to-digital converters (ADCs) at instants $t = \tau_{ni} + kT_r, k = 1, 2, \ldots, K$

$$\begin{aligned} x_{ni}(k) &= x_{ni}(t)|_{t=\tau_{ni}+kT_r} \\ &= \sum_{m=0}^{M-1} \tilde{\alpha}_{nm} e^{-j2\pi f_0 \tau_{nm}} e^{j(\psi_m - \psi_i)} \\ &\quad \times \chi_{mi}(\tau_{ni} - \tau_{nm}, f_{nm}) e^{j2\pi k f_{nm} T_r} \\ &= \tilde{\alpha}_{ni} e^{-j2\pi f_0 \tau_{ni}} \chi_{ii}(0, f_{ni}) e^{j2\pi k f_{ni} T_r} \\ &\quad + \sum_{m \neq i} \tilde{\alpha}_{nm} e^{-j2\pi f_0 \tau_{nm}} e^{j(\psi_m - \psi_i)} \\ &\quad \times \chi_{mi}(\tau_{ni} - \tau_{nm}, f_{nm}) e^{j2\pi k f_{nm} T_r}, \end{aligned} \tag{11}$$

where τ_{ni} needs to be aligned over different Tx-Rx pairs to make sure all Tx-Rx pairs probe the target at the same range bin. Therefore, $\{x_{ni}(k)\}, k = 1, 2, \ldots, K$, represent K slow-time samples corresponding to a target at a given range bin for all Tx-Rx pairs. It is seen that the output of the i-th matched filter $x_{ni}(k)$ consists of M components: the first term is the *auto-component* between the i-th transmit waveform and the i-th matched filter, and the other term sums up the *cross-components* residuals between the remaining $M-1$ transmit waveforms and the i-th matched filter.

B. Modeling of Target Residuals Due to Imperfect Waveform Separation

Current studies usually assume that the mutual orthogonality across different waveforms holds everywhere in the range-Doppler plane, i.e., $\chi_{mi}(\tau_{ni} - \tau_{nm}, f_{nm}) = 0$ in (11), and none of these cross-components are present at outputs of matched filter banks. However, this assumption cannot be met in practice [33], [34]. As also shown in [36], [37], the largest range-Doppler area without ambiguity ("the clean area") is reduced from $(\Delta\tau \Delta f_d)_{\max} = 1$ for a singe-waveform radar to $1/M$ for MIMO radar using M orthogonal waveforms. It quantitatively confirms that the zero cross-components for the MIMO radar case is only possible for smaller Doppler velocities and time delays than the traditional phased array radar with coherent waveforms. In the following, we model the outputs of matched filters consisting of a target signal and a target residual with a subspace structure.

Stacking the K discrete samples into a vector and defining $\bar{\alpha}_{nm} = \tilde{\alpha}_{nm} e^{-j2\pi f_0 \tau_{nm}} \chi_{mi}(\tau_{ni} - \tau_{nm}, f_{nm})$, we have

$$\mathbf{x}_{ni} = \bar{\alpha}_{ni} \mathbf{s}(f_{ni}) + \sum_{m \neq i} \bar{\alpha}_{nm} e^{j(\psi_m - \psi_i)} \mathbf{s}(f_{nm}), \tag{12}$$

where $\mathbf{s}(f) \triangleq [1, e^{j2\pi f T_r}, \ldots, e^{j2\pi(K-1) f T_r}]^T$. This can be written as in a matrix form

$$\mathbf{x}_{ni} = \bar{\alpha}_{ni} \mathbf{s}(f_{ni}) + \mathbf{H}_{ni} \boldsymbol{\theta}_{ni}, \tag{13}$$

where the subspace matrix is of dimension $K \times (M-1)$

$$\mathbf{H}_{ni} = [\mathbf{s}(f_{n1}), \ldots, \{\mathbf{s}(f_{nm})\}_{m \neq i}, \ldots, \mathbf{s}(f_{nM})], \tag{14}$$

and the subspace coefficient vector is given as

$$\boldsymbol{\theta}_{ni} = \begin{bmatrix} \bar{\alpha}_{n1} e^{j(\psi_1 - \psi_i)} \\ \vdots \\ \{\bar{\alpha}_{nm} e^{j(\psi_m - \psi_i)}\}_{m \neq i} \\ \vdots \\ \bar{\alpha}_{nM} e^{j(\psi_M - \psi_i)} \end{bmatrix}. \tag{15}$$

From (12), it is seen that the target signal has an *unknown* amplitude $\bar{\alpha}_{ni}$ and a steering vector $\mathbf{s}(f_{ni})$ at the corresponding (n,i)-th bistatic Doppler frequency f_{ni}. Meanwhile, the target residual due to imperfect waveform separation is shown to fall within an $(M-1)$ subspace spanned by $(M-1)$ steering vectors at the other $(M-1)$ bistatic Doppler frequencies $\{f_{nm}\}_{m \neq i}$.

Remark: It is seen from (12) that the residual amplitude $\bar{\alpha}_{nm}$ is a function of the ambiguity function $\chi_{mi}(\tau_{ni} - \tau_{nm}, f_{nm})$ at given delay difference $\tau_{ni} - \tau_{nm}$ and Doppler frequency f_{nm}.

Authorized licensed use limited to: Stevens Institute of Technology. Downloaded on August 18,2020 at 19:27:31 UTC from IEEE Xplore. Restrictions apply.

As a result, the minimum possible residual can be determined by the highest sidelobe in the ambiguity function which is a function of the used orthogonal waveforms. If one has prior knowledge on possible locations (τ_{nm}) and velocities f_{nm}, the minimum possible residual may be confined to the local maximum value of the ambiguity function over the possible delay-Doppler area. In case that the local maximum is negligible, the residual amplitude $\{\bar{\alpha}_{nm}\}_{m\neq i}$ may be negligible compared with the target amplitude $\bar{\alpha}_{ni}$.

With N receivers and M matched filters at each receiver, the overall received signals are $\mathbf{x}_{ni}, i = 1, 2, \ldots, M, n = 1, \ldots, N$.

III. Problem Formulation of Moving Target Detection

In the following, we formulate moving target detection as a binary hypothesis testing problem by explicitly accounting for the target residual described in the above section.

A. Problem Formulation

In addition to the target signal and its residual, the disturbance signal due to ground clutter, jamming signals and thermal noise is present in the received signal. It is generally assumed that the disturbance component for the (n, i)-th Tx-Rx pair, $\mathbf{w}_{ni}$, has a complex Gaussian distribution with zero mean and covariance matrix $\mathbf{R}_{ni}$, i.e., $\mathbf{w}_{ni} \sim \mathcal{CN}(\mathbf{0}, \mathbf{R}_{ni})$.

With the above modeling, the moving target detection with the distributed MIMO radar is then formulated as the following binary hypothesis testing problem:

$$\begin{aligned} H_0: &\quad \mathbf{x}_{ni} = \mathbf{w}_{ni}, \\ H_1: &\quad \mathbf{x}_{ni} = \alpha_{ni}\mathbf{s}(f_{ni}) + \mathbf{H}_{ni}\boldsymbol{\theta}_{ni} + \mathbf{w}_{ni}, \\ &\qquad n = 1, \ldots, N; \quad i = 1, \ldots, M, \end{aligned} \tag{16}$$

where $\mathbf{x}_{ni}$ is the output of the i-th (out of M) matched filter at the n-th receiver, α_{ni} is the unknown amplitude, $\boldsymbol{\theta}_{ni}$ is the target residual coefficient, $\mathbf{H}_{ni}$ is the target residual steering matrix of (14), and the disturbance $\mathbf{w}_{ni} \sim \mathcal{CN}(\mathbf{0}, \mathbf{R}_{ni})$. We further assume that the range spaces of $\mathbf{s}$ and $\mathbf{H}$ are linearly independent, since all M Doppler frequencies are bi-static projections of the same target Doppler frequency onto M transmitting angles (and the same receiving angle) in the view of (5) and (13). In addition to the test signal, G target-free training signals $\mathbf{g}_{ni}(g), g = 1, \ldots, G$, are available from neighboring range cells. The purpose here is to detect if the target signal is present in the MN matched filter outputs while exploiting the subspace target residual whose existence is associated with the target signal of interest.

B. Distributed First-Order Gaussian Model - DFOG

First, we model both the target amplitude α_{ni} and residual coefficient $\boldsymbol{\theta}_{ni}$ as deterministic unknown parameters. In other words, we assume the RCSs are different from different Tx-Rx pairs but *non-fluctuating* from pulse to pulse throughout a single scan (e.g., Swirling model I). With this assumption, we can group the signal steering vector and residual subspace as an expanded subspace $\mathbf{S}_{ni} = [\mathbf{s}_{ni}, \mathbf{H}_{ni}]$ and the unknown coefficient $\boldsymbol{\beta} = [\alpha_{ni}, \boldsymbol{\theta}_{ni}^T]^T$. As a result, we have the following distributed first-order Gaussian (DFOG) model:

$$\begin{aligned} H_0: &\quad \mathbf{x}_{ni} = \mathbf{w}_{ni}, \quad n = 1, \ldots, N, \quad i = 1, \ldots, M, \\ H_1: &\quad \mathbf{x}_{ni} = \mathbf{S}_{ni}\boldsymbol{\beta}_{ni} + \mathbf{w}_{ni}, \end{aligned} \tag{17}$$

where one needs to determine if the subspace signal is present or not.

It is easy to recognize that (17) is an extension of the FOG model of the MTD with colocated phased array of $N = 1$ and $M = 1$. One can readily apply classical solutions such as matched subspace detectors [38], adaptive subspace detector (ASD) [39], the Kelly's GLRT [40], and the adaptive coherence estimator (ACE) [39], [41], [42] with $\mathbf{R}$ estimated from the G training signals. The distributed GLRT for the DFOG model has been considered in [6].

C. Distributed Second-Order Gaussian Model - DSOG

In the case of *fluctuating* RCS from pulse to pulse (e.g., Swerling model IV), we assume the target amplitude α_{ni} and the subspace coefficient $\boldsymbol{\theta}_{ni}$ are random parameters. As a result, we have the following distributed second-order Gaussian (DSOG) model where the signal of interest is a random subspace signal

$$\begin{aligned} H_0: &\quad \mathbf{x}_{ni} = \mathbf{w}_{ni}, \quad n = 1, \ldots, N; \quad i = 1, \ldots, M, \\ H_1: &\quad \mathbf{x}_{ni} = \mathbf{S}_{ni}\boldsymbol{\gamma}_{ni} + \mathbf{w}_{ni}, \end{aligned} \tag{18}$$

where $\boldsymbol{\gamma}_{ni} = [\alpha_{ni}, \boldsymbol{\theta}_{ni}^T]^T \sim \mathcal{CN}(\mathbf{0}_M, \boldsymbol{\Gamma}_{ni})$ with $\mathbf{0}_M$ denoting an all-zero vector of dimension M and $\boldsymbol{\Gamma}_{ni} \in \mathbb{C}^{M\times M}$ denoting the covariance matrix. It is easy to see that (18) is an extension of the traditional SOG model considered in [43]. The detection problem in the SOG model was solved from a GLRT principle in [43].

D. Distributed Hybrid-Order (First-Order and Second-Order) Gaussian Model - DHOG

Finally, we consider a hybrid case where the target amplitude α_{ni} follows a non-fluctuating model while the target residual $\boldsymbol{\theta}_{ni}$ are fluctuating from pulse to pulse due to the phase mismatch $\phi_m - \phi_i$ in (15). As a result, α_{ni} are treated as deterministic unknown parameters while $\boldsymbol{\theta}_{ni}$ are modeled as random parameters, leading to

$$\begin{aligned} H_0: &\quad \mathbf{x}_{ni} = \mathbf{w}_{ni}, \quad n = 1, \ldots, N; \quad i = 1, \ldots, M, \\ H_1: &\quad \mathbf{x}_{ni} = \alpha_{ni}\mathbf{s}(f_{ni}) + \mathbf{H}_{ni}\boldsymbol{\theta}_{ni} + \mathbf{w}_{ni}, \end{aligned} \tag{19}$$

where $\boldsymbol{\theta}_{ni} \sim \mathcal{CN}(\mathbf{0}, \boldsymbol{\Sigma}_{ni})$ with $\boldsymbol{\Sigma}_{ni}$ denoting the unknown residual subspace covariance matrix and α_{ni} is deterministic unknown. Unlike the DFOG and DSOG models, the DHOG model distinguishes the two hypotheses not only in the first-order statistic but also the second-order statistic of the received signal. It is worth noting that such a hybrid model may be useful to represent a compound cluster of scatterers, a portion of which exhibit *non-fluctuating* reflection characteristics while the others show more rapid *fluctuating* reflection characteristics during a CPI.

Authorized licensed use limited to: Stevens Institute of Technology. Downloaded on August 18,2020 at 19:27:31 UTC from IEEE Xplore. Restrictions apply.

Given knowledge of the residual subspace $\mathbf{H}_{ni}$, one is tempted to project the observation $\mathbf{x}_{ni}$ to the subspace orthogonal to $\mathbf{H}_{ni}$, which eliminates the residual interference, and then apply the conventional matched filter to the projected signal for target detection. Note that the projection is an irreversible compression process that will lead to a loss of the signal energy (unless the signal steering vector lies in the orthogonal subspace). This resulting detector, henceforth referred to as the projection matched filter (PMF), is in general suboptimal. In the following, we introduce an alternative and better solution by jointly estimating the parameters associated with the signal and residual interference.

IV. Proposed Distributed GLRT

In this section, we assume the target velocity is known. It is standard in radar signal detection to divide the uncertainty region of the target velocity or Doppler frequency into small cells and each is tested for the presence of target [45]. Therefore, we drop the dependence of $\mathbf{s}$ on f_{ni} herein. We adopt a two-step approach (like the AMF [46]) to develop the distributed MTD scheme based on the DHOG model in (19). First, we develop a distributed GLRT for (19) by assuming that the disturbance covariance matrix $\mathbf{R}_{ni}$ is known. Then, $\mathbf{R}_{ni}$ in the test statistic is replaced by its sample covariance matrices from training signals.

A. The GLRT Principle

The GLRT principle for (19) requires the ML estimates of the unknown parameters including the target amplitudes α_{ni} and the subspace covariance matrices $\mathbf{\Sigma}_{ni}$. Invoking the statistical independence across multiple Tx-Rx pairs, the MIMO-GLRT detector takes the form of

$$T = \frac{\prod_{n,i} \max\limits_{\alpha_{ni},\mathbf{\Sigma}_{ni}} f_1(\mathbf{x}_{ni}\,|\alpha_{ni},\mathbf{\Sigma}_{ni})}{\prod_{n,i} f_0(\mathbf{x}_{ni})}, \tag{20}$$

where $f_1(\mathbf{x}_{ni}\,|\alpha_{ni},\mathbf{\Sigma}_{ni})$ and $f_0(\mathbf{x}_{ni})$ denote the likelihood functions for the (n,i)-th Tx-Rx pair under H_1 and H_0, respectively. With known $\mathbf{R}_{ni}$, we can apply a pre-whitening process, i.e., $\mathbf{y}_{ni} = \mathbf{R}_{ni}^{-1/2}\mathbf{x}_{ni}$, to convert the problem of interest (19) to an equivalent binary hypothesis testing as

$$\begin{aligned} H_0:&\quad \mathbf{y}_{ni} \sim \mathcal{CN}(\mathbf{0},\mathbf{I}),\\ H_1:&\quad \mathbf{y}_{ni} \sim \mathcal{CN}(\alpha_{ni}\tilde{\mathbf{s}}_{ni}, \tilde{\mathbf{H}}_{ni}\mathbf{\Sigma}_{ni}\tilde{\mathbf{H}}_{ni}^H + \mathbf{I}), \end{aligned} \tag{21}$$

where $\tilde{\mathbf{s}}_{ni} = \mathbf{R}_{ni}^{-1/2}\mathbf{s}_{ni}$, $\tilde{\mathbf{H}}_{ni} = \mathbf{R}_{ni}^{-1/2}\mathbf{H}_{ni}$ and the disturbance covariance matrix is an identity matrix due to the pre-whitening process.

It is clear that all unknown parameters, i.e, $\mathbf{\Sigma}_{ni}$ and α_{ni}, are both under the alternative hypothesis, whereas there is no unknown parameters in the null hypothesis. Subsequently, the MIMO-GLRT detector takes the form of

$$T = \prod_{n,i} T_{ni} = \prod_{n,i} \frac{\max\limits_{\alpha_{ni},\mathbf{\Sigma}_{ni}} f_1(\mathbf{y}_{ni}\,|\alpha_{ni},\mathbf{\Sigma}_{ni})}{f_0(\mathbf{y}_{ni})}, \tag{22}$$

where T_{ni} is the test statistic of local GLRT at one Tx-Rx pair, $f_1(\mathbf{y}_{ni}\,|\alpha_{ni},\mathbf{\Sigma}_{ni})$ and $f_0(\mathbf{y}_{ni})$ are, respectively, the likelihood function of the whitened signal for the (n,i)-th Tx-Rx pair under both hypotheses:

$$\begin{aligned} f_1(\mathbf{y}_{ni}\,|\alpha_{ni},\mathbf{\Sigma}_{ni}) &= \frac{e^{-(\mathbf{y}_{ni}-\alpha_{ni}\tilde{\mathbf{s}}_{ni})^H\mathbf{C}_{ni}^{-1}(\mathbf{y}_{ni}-\alpha_{ni}\tilde{\mathbf{s}}_{ni})}}{\pi^K\,|\mathbf{C}_{ni}|},\\ f_0(\mathbf{y}_{ni}) &= \frac{e^{-\mathbf{y}_{ni}^H\mathbf{y}_{ni}}}{\pi^K}, \end{aligned} \tag{23}$$

with $\mathbf{C}_{ni} \triangleq \tilde{\mathbf{H}}_{ni}\mathbf{\Sigma}_{ni}\tilde{\mathbf{H}}_{ni}^H + \mathbf{I} \succ \mathbf{I}$ implying $\mathbf{\Sigma}_{ni}$ is positive definite, and $|\mathbf{C}|$ denoting the determinant of the matrix $\mathbf{C}$.

In the next two subsections, we derive the ML estimates of the subspace covariance matrix $\mathbf{\Sigma}_{ni}$ and the amplitude α_{ni}. Then, we develop the test statistic of the local GLRT T_{ni}, followed by the derivation of the distributed GLRT T.

B. Local ML Estimation of the Residual Covariance $\mathbf{\Sigma}_{ni}$

As seen in (22), the maximization over $\mathbf{\Sigma}_{ni}$ and α_{ni} can be performed separately over each Tx-Rx pair. Therefore, we drop the index $(\cdot)_{ni}$ of Tx-Rx pairs for notation simplicity.

Note that $\mathbf{C} = \tilde{\mathbf{H}}\mathbf{\Sigma}\tilde{\mathbf{H}}^H + \mathbf{I}$. To compute $|\mathbf{C}|$ and $\mathbf{C}^{-1}$ in the local likelihood function of (23) under the alternative hypothesis, we first represent the subspace term as

$$\tilde{\mathbf{H}}\mathbf{\Sigma}\tilde{\mathbf{H}}^H = \bar{\mathbf{H}}\mathbf{E}\bar{\mathbf{H}}^H, \tag{24}$$

where

$$\bar{\mathbf{H}} = \tilde{\mathbf{H}}(\tilde{\mathbf{H}}^H\tilde{\mathbf{H}})^{-1/2}\mathbf{U}, \tag{25}$$

is a $K \times r$ matrix with $r = (M-1)$ orthonormal columns, $\mathbf{U} \in \mathbb{C}^{r\times r}$ is an unitary matrix and $\mathbf{E} \in \mathbb{R}^{r\times r}$ is a diagonal matrix with e_i denoting its i-th diagonal element. Equivalently, the residual covariance matrix is represented by the unitary matrix $\bar{\mathbf{H}}$ and the diagonal matrix $\mathbf{E}$. With (24), we have

$$\begin{aligned} \mathbf{C}^{-1} &= \bar{\mathbf{H}}\left(\mathbf{E}+\mathbf{I}\right)^{-1}\bar{\mathbf{H}}^H + \bar{\mathbf{H}}^{\perp}\bar{\mathbf{H}}^{\perp H}\\ &= \bar{\mathbf{H}}\left(\mathbf{E}+\mathbf{I}\right)^{-1}\bar{\mathbf{H}}^H + \left(\mathbf{I} - \mathbf{P}_{\bar{\mathbf{H}}}\right), \end{aligned} \tag{26}$$

$$|\mathbf{C}| = \prod_{i=1}^{r}(e_i+1). \tag{27}$$

Remark: Essentially, the unitary matrix $\mathbf{U}$ plays as a rotation matrix in the subspace $\langle\bar{\mathbf{H}}\rangle$ spanned by the (orthonormalized) columns of $\tilde{\mathbf{H}}$. This can be seen from the fact that the projection matrix $\mathbf{P}_{\tilde{\mathbf{H}}}$ in (26)

$$\mathbf{P}_{\bar{\mathbf{H}}} = \bar{\mathbf{H}}\left(\bar{\mathbf{H}}^H\bar{\mathbf{H}}\right)^{-1}\bar{\mathbf{H}}^H = \tilde{\mathbf{H}}(\tilde{\mathbf{H}}^H\tilde{\mathbf{H}})^{-1}\tilde{\mathbf{H}}^H = \mathbf{P}_{\tilde{\mathbf{H}}}, \tag{28}$$

is the same as the projection matrix $\mathbf{P}_{\bar{\mathbf{H}}}$, which is hence independent of the rotation matrix $\mathbf{U}$. In other words, $\langle\bar{\mathbf{H}}\rangle = \langle\tilde{\mathbf{H}}\rangle$.

Define

$$\mathbf{z} \stackrel{\triangle}{=} \begin{bmatrix}\bar{\mathbf{H}} & \bar{\mathbf{H}}^{\perp}\end{bmatrix}^H(\mathbf{y}-\alpha\tilde{\mathbf{s}}), \tag{29}$$

and denote z_i as its i-th element. With the help of (26) and (27), the negative log-likelihood function (NLLF) under H_1, i.e., $f_1(\mathbf{y}|\alpha,\mathbf{\Sigma})$ in (23), can be expressed as

$$\begin{aligned} -\ln f_1(\mathbf{y}\,|\alpha,\mathbf{E},\bar{\mathbf{H}}) &\propto \ln|\mathbf{C}| + (\mathbf{y}-\alpha\tilde{\mathbf{s}})^H\mathbf{C}^{-1}(\mathbf{y}-\alpha\tilde{\mathbf{s}})\\ &\propto \sum_{i=1}^{r}\ln(e_i+1) + \sum_{i=1}^{r}\frac{|z_i|^2}{e_i+1} + \sum_{i=r+1}^{K}|z_i|^2. \end{aligned} \tag{30}$$

Authorized licensed use limited to: Stevens Institute of Technology. Downloaded on August 18,2020 at 19:27:31 UTC from IEEE Xplore. Restrictions apply.

The ML estimate of $\mathbf{E}$ can be obtained by taking the derivative of the NLLF with respect to e_i and equating it to zero, i.e.,

$$\hat{e}_i = \max\left\{|z_i|^2 - 1, 0\right\}, \quad i = 1, 2, \ldots, r. \tag{31}$$

With the ML estimate of $\mathbf{E}$, the NLLF (30) reduces to

$$\sum_{\substack{1\le i\le r:\\ |z_i|^2\le 1}} |z_i|^2 + \sum_{\substack{1\le i\le r:\\ |z_i|^2> 1}} \left(\ln|z_i|^2 + 1\right) + \sum_{i=r+1}^{K} |z_i|^2. \tag{32}$$

The next step is to derive the ML estimate of $\bar{\mathbf{H}}$ which is equivalent to the ML estimate of $\mathbf{U}$ according to (25). Note that the last term of the NLLF (32) reflects the energy of the whitened target-free observed signal $(\mathbf{y} - \alpha\tilde{\mathbf{s}})$ projected into the orthogonal complement space of $\langle\tilde{\mathbf{H}}\rangle$

$$\begin{aligned}\sum_{i=r+1}^{K} |z_i|^2 &= (\mathbf{y} - \alpha\tilde{\mathbf{s}})^H \bar{\mathbf{H}}^{\perp}\bar{\mathbf{H}}^{\perp H}(\mathbf{y} - \alpha\tilde{\mathbf{s}}) \\ &= (\mathbf{y} - \alpha\tilde{\mathbf{s}})^H (\mathbf{I} - \mathbf{P}_{\tilde{\mathbf{H}}})(\mathbf{y} - \alpha\tilde{\mathbf{s}}),\end{aligned} \tag{33}$$

which is hence independent of the rotation matrix $\mathbf{U}$.

With these observations, the ML estimate of $\mathbf{U}$ is obtained by minimizing the sum of the first two terms (32) w.r.t. $\mathbf{U}$:

$$\sum_{\substack{1\le i\le r:\\ |z_i|^2\le 1}} |z_i|^2 + \sum_{\substack{1\le i\le r:\\ |z_i|^2> 1}} \left(\ln|z_i|^2 + 1\right). \tag{34}$$

Denote $\eta = \sum_{1\le i\le r} |z_i|^2$. It is noted that

$$\begin{aligned}\eta &= \sum_{1\le i\le r} |z_i|^2 = (\mathbf{y} - \alpha\tilde{\mathbf{s}})^H \bar{\mathbf{H}}\bar{\mathbf{H}}^H (\mathbf{y} - \alpha\tilde{\mathbf{s}}) \\ &= (\mathbf{y} - \alpha\tilde{\mathbf{s}})^H \mathbf{P}_{\bar{\mathbf{H}}} (\mathbf{y} - \alpha\tilde{\mathbf{s}}),\end{aligned} \tag{35}$$

is also independent of the rotation matrix $\mathbf{U}$. Depending on the value of η, the ML estimate of $\mathbf{U}$ (or, equivalently, $\bar{\mathbf{H}}$) can be obtained as

- $\eta < 1$: $\eta < 1$ implies that $|z_i|^2 < 1, i = 1, 2, \ldots, r$. The cost function (34) reduces to

$$\sum_{i=1}^{r} |z_i|^2 = \eta, \tag{36}$$

  which is hence independent of $\mathbf{U}$ (see also (35)). Therefore, in this case, $\mathbf{U}$ can be an arbitrary $r \times r$ unitary matrix. And the NLLF (32) reduces to

$$\sum_{i=1}^{r} |z_i|^2 + \sum_{i=r+1}^{K} |z_i|^2 = \|\mathbf{y} - \alpha\tilde{\mathbf{s}}\|^2. \tag{37}$$

- $\eta \ge 1$: The ML estimate of $\bar{\mathbf{H}}$ is a matrix with one column given by (without loss of generality, we assume the first column)

$$\hat{\bar{\mathbf{H}}}_{\text{ML}}[:, 1] = \frac{\mathbf{P}_{\tilde{\mathbf{H}}}(\mathbf{y} - \alpha\tilde{\mathbf{s}})}{\|\mathbf{P}_{\tilde{\mathbf{H}}}(\mathbf{y} - \alpha\tilde{\mathbf{s}})\|}, \tag{38}$$

  and the remaining $(r-1)$ columns are orthonormal to $\hat{\bar{\mathbf{H}}}_{\text{ML}}[:, 1]$. It follows $\mathbf{z}_r = [\sqrt{\eta}, 0, \ldots, 0]^T$. The proof can be found in [44, Section. II.B, Appendix]). Geometrically, in this case, we choose the rotation matrix $\mathbf{U}$ which rotates the coordinate in $\langle\tilde{\mathbf{H}}\rangle$ such that one axis aligns perfectly with the projection of $(\mathbf{y} - \alpha\tilde{\mathbf{s}})$ into $\langle\tilde{\mathbf{H}}\rangle$. Then, the NLLF (32) reduces to

$$\begin{aligned}\ln|z_1|^2 + 1 + \sum_{i=r+1}^{K} |z_i|^2 &= \ln\eta + 1 + \sum_{i=r+1}^{K} |z_i|^2 \\ &= \ln(\mathbf{y} - \alpha\tilde{\mathbf{s}})^H \mathbf{P}_{\tilde{\mathbf{H}}} (\mathbf{y} - \alpha\tilde{\mathbf{s}}) + 1 \\ &\quad + (\mathbf{y} - \alpha\tilde{\mathbf{s}})^H (\mathbf{I} - \mathbf{P}_{\tilde{\mathbf{H}}})(\mathbf{y} - \alpha\tilde{\mathbf{s}}).\end{aligned} \tag{39}$$

The above ML estimates of $\mathbf{E}$ and $\bar{\mathbf{H}}$ are based on a given amplitude α. The next step is to find the ML estimate of α.

C. Local ML Estimation of Amplitude α

In this subsection, we develop the *exact* ML estimate of α, which is different from the *ad hoc* solution in [44]. Due to the condition on η for the ML estimate of $\bar{\mathbf{H}}$, the cost function for the ML estimate of α is a composite function which combines two sub-functions given by (37) and (39), respectively. More precisely, we have the cost function for the ML estimate of α

$$g(\alpha) = \begin{cases} g_1(\alpha), & \text{if } \alpha \in \Psi_1 \\ g_2(\alpha), & \text{if } \alpha \in \Psi_2 \end{cases}, \tag{40}$$

where

$$g_1(\alpha) = \|\mathbf{y} - \alpha\tilde{\mathbf{s}}\|^2, \tag{41}$$

$$g_2(\alpha) = \ln\|\mathbf{P}_{\tilde{\mathbf{H}}}(\mathbf{y} - \alpha\tilde{\mathbf{s}})\|^2 + 1 + \left\|\mathbf{P}^{\perp}_{\tilde{\mathbf{H}}}(\mathbf{y} - \alpha\tilde{\mathbf{s}})\right\|^2, \tag{42}$$

and

$$\Psi_1 = \{\alpha \in \mathbb{C} : \eta(\alpha) \le 1\}, \tag{43}$$

$$\Psi_2 = \{\alpha \in \mathbb{C} : \eta(\alpha) \ge 1\}, \tag{44}$$

with

$$\eta(\alpha) = \|\mathbf{P}_{\tilde{\mathbf{H}}}(\mathbf{y} - \alpha\tilde{\mathbf{s}})\|^2. \tag{45}$$

1) Geometry of Ψ_1 and Ψ_2: It is easy to see that the feasible set Ψ_1 of (43) is a disk centered at α_{Ψ_1} with radius r_{Ψ_1} while Ψ_2 complements Ψ_1 in the complex-valued domain. As shown in Fig. 2, the center and radius of Ψ_1 are given, respectively, by

$$\alpha_1 = \alpha_{\Psi_1} = \frac{\mathbf{s}^H \mathbf{P}_{\tilde{\mathbf{H}}}\mathbf{y}}{\mathbf{s}^H \mathbf{P}_{\tilde{\mathbf{H}}}\mathbf{s}}, \tag{46}$$

$$r_{\Psi_1} = \frac{\sqrt{e - a}}{e}, \tag{47}$$

where

$$a = \|\mathbf{P}_{\tilde{\mathbf{H}}}\mathbf{y}\|^2 \|\mathbf{P}_{\tilde{\mathbf{H}}}\tilde{\mathbf{s}}\|^2 - \left\|\tilde{\mathbf{s}}^H \mathbf{P}_{\tilde{\mathbf{H}}}\mathbf{y}\right\|^2, \tag{48}$$

$$e = \|\mathbf{P}_{\tilde{\mathbf{H}}}\tilde{\mathbf{s}}\|^2. \tag{49}$$

It is worth noting that the feasible sets Ψ_1 and Ψ_2 are *adaptively* determined by the (whitened) observed signal $\mathbf{y}$, the (whitened) subspace matrix $\tilde{\mathbf{H}}$ and the (whitened) steering vector $\tilde{\mathbf{s}}$. Therefore, they are fully determined by observed signals but may vary from one scan to another scan.

Authorized licensed use limited to: Stevens Institute of Technology. Downloaded on August 18,2020 at 19:27:31 UTC from IEEE Xplore. Restrictions apply.

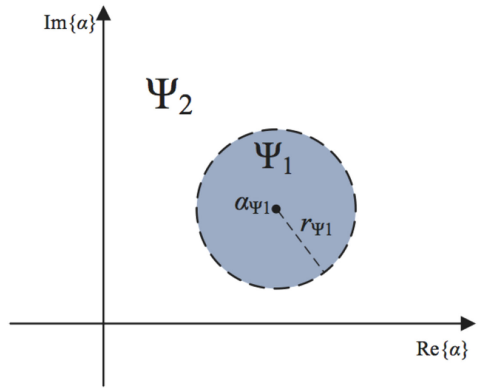

Fig. 2. Feasible areas of the cost function $g(\alpha)$ for the ML estimate of the amplitude α.

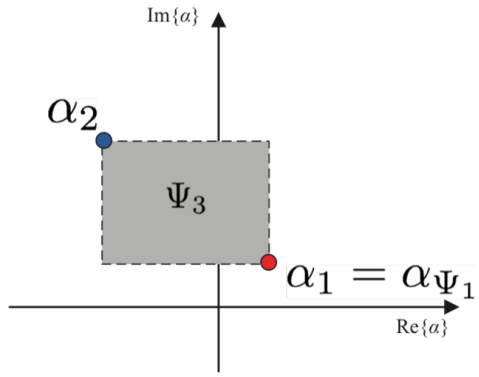

Fig. 3. The solution region of unconstrained $g_2(\alpha)$.

2) Solutions to Unconstrained $g_1(\alpha)$ and $g_2(\alpha)$: Before we move to the ML estimation of the amplitude, let us first look at the unconstrained optimization of $g_1(\alpha)$ and $g_2(\alpha)$.

To minimize $g_1(\alpha) = \|\mathbf{y} - \alpha\tilde{\mathbf{s}}\|^2$, the solution to unconstrained $g_1(\alpha)$ is

$$\alpha_3 = \frac{\tilde{\mathbf{s}}^H\mathbf{y}}{\tilde{\mathbf{s}}^H\tilde{\mathbf{s}}}. \tag{50}$$

To minimize $g_2(\alpha)$ of (42), we notice that it consists of two α-related terms:

- the term $d_1(\alpha) \stackrel{\triangle}{=} \ln\|\mathbf{P}_{\tilde{\mathbf{H}}}(\mathbf{y} - \alpha\tilde{\mathbf{s}})\|^2 + 1$ that is minimized at

$$\alpha_1 = \frac{\mathbf{s}^H\mathbf{P}_{\tilde{\mathbf{H}}}\mathbf{y}}{\mathbf{s}^H\mathbf{P}_{\tilde{\mathbf{H}}}\mathbf{s}} \Rightarrow \alpha_1 = \alpha_{\Psi_1}, \tag{51}$$

  which is also the center α_{Ψ_1} of the feasible set Ψ_1; see Fig. 3.

- the term $d_2(\alpha) \stackrel{\triangle}{=} \|\mathbf{P}^{\perp}_{\tilde{\mathbf{H}}}(\mathbf{y} - \alpha\tilde{\mathbf{s}})\|^2$ that is a quadratic function minimized at

$$\alpha_2 = \frac{\mathbf{s}^H\mathbf{P}^{\perp}_{\tilde{\mathbf{H}}}\mathbf{y}}{\mathbf{s}^H\mathbf{P}^{\perp}_{\tilde{\mathbf{H}}}\mathbf{s}}. \tag{52}$$

Both d_1 and d_2 are monotonically increasing w.r.t. α when α moves away from the corresponding minimizer α_1 or α_2. Therefore, the solution to the unconstrained $g_2(\alpha)$ falls within a *square* area cornered at α_1 and α_2 in the two-dimensional complex-valued domain; see the shaded square in Fig. 3 for illustration. Without of losing generality, we assume $\Re\{\alpha_1\} > \Re\{\alpha_2\}$ and $\Im\{\alpha_2\} > \Im\{\alpha_1\}$ and denote the square area as

$$\Psi_3 = \{\alpha \in \mathbb{C} : \Re\{\alpha_2\} \le \Re\{\alpha\} \le \Re\{\alpha_1\}, \Im\{\alpha_1\} \le \Im\{\alpha\} \le \Im\{\alpha_2\}\}. \tag{53}$$

3) Local ML Estimation of Amplitude: Depending on the geometry of Ψ_1 and Ψ_2, we have the following cases to develop the ML estimate of α:

Case I ($\Psi_1 = \emptyset$ and $\Psi_2 = \mathbb{C}$): Let us look at one extreme case when the feasible set Ψ_1 is an empty set and Ψ_2 covers all complex-valued domain. In this case, the cost function $g(\alpha)$ of (40) reduces to the unconstrained $g_2(\alpha)$. As stated above, the solution to the unconstrained $g_2(\alpha)$ is confined in the set Ψ_3. It can be effectively found by a gradient descent method initiated at either α_1 or α_2.

The existence of Case I can be determined by the following sufficient condition (recall the geometry of Ψ_1 and Ψ_2)

$$a \ge e \text{ and } e < \infty \quad \Rightarrow \quad r_{\Psi_1} \le 0. \tag{54}$$

The condition of $e = \|\mathbf{P}_{\tilde{\mathbf{H}}}\tilde{\mathbf{s}}\|^2 < \infty$ is satisfied as long as the steer vector $\mathbf{s}$ has a finite energy, since e reflects the energy of the whitened steering vector $\tilde{\mathbf{s}}$ projected into the whitened subspace $\langle\tilde{\mathbf{H}}\rangle$. The other condition of $a \ge e$ can be checked as

$$a \ge e \Rightarrow \|\mathbf{P}_{\tilde{\mathbf{H}}}\mathbf{y}\|^2\|\mathbf{P}_{\tilde{\mathbf{H}}}\tilde{\mathbf{s}}\|^2 \ge \left|\tilde{\mathbf{s}}^H\mathbf{P}_{\tilde{\mathbf{H}}}\mathbf{y}\right|^2 + \|\mathbf{P}_{\tilde{\mathbf{H}}}\tilde{\mathbf{s}}\|^2, \tag{55}$$

once the observed signal, steering vector and residual subspace are given.

Case II ($\Psi_1 = \mathbb{C}$ and $\Psi_2 = \emptyset$): On the other hand, Ψ_1 can expand to the whole complex-valued domain while Ψ_2 vanishes to an empty set. Correspondingly, the cost function $g(\alpha)$ of (40) reduces to the unconstrained $g_1(\alpha)$. As also stated above, the solution to the unconstrained $g_1(\alpha)$ is given by α_3 of (50).

The existence of Case II can be readily checked as

$$e = \|\mathbf{P}_{\tilde{\mathbf{H}}}\tilde{\mathbf{s}}\|^2 = 0 \quad \Rightarrow \quad r_{\Psi_1} = \infty, \tag{56}$$

which is equivalent to saying that the whitened subspace $\langle\tilde{\mathbf{H}}\rangle$ is orthogonal to the whitened steering vector $\langle\tilde{\mathbf{s}}\rangle$, i.e.,

$$\langle\tilde{\mathbf{H}}\rangle \perp \langle\tilde{\mathbf{s}}\rangle. \tag{57}$$

In the considered distributed MIMO scenario, the condition of $\langle\tilde{\mathbf{H}}\rangle \perp \langle\tilde{\mathbf{s}}\rangle$ implies that $\mathbf{s}(f_{ni})$ is completely orthogonal to its target residual subspace $\tilde{\mathbf{H}}$ of (14) formed by other $(M-1)$ Doppler frequencies $\mathbf{s}(f_{nm})$ with $m \ne i$. Since all M Doppler frequencies are bi-static projection of the same target Doppler frequency onto M transmitting angles (and the same receiving angle), it is highly unlikely that $\langle\tilde{\mathbf{H}}\rangle \perp \langle\tilde{\mathbf{s}}\rangle$ holds.

Case III ($\Psi_1 \ne \emptyset$ and $\Psi_2 \ne \emptyset$): When neither Ψ_1 nor Ψ_2 is an empty set, we need to evaluate the two constrained cost functions: $g_1(\alpha)$ over Ψ_1 and $g_2(\alpha)$ over Ψ_2, then compare the two minimum values, and find the global minimum for $g(\alpha)$. Further depending on the geometry of Ψ_2 and α_3, we have the following two scenarios in Case III (see Fig 4):

- Scenario A ($\Psi_2 \cap \Psi_3 \ne \emptyset$): As shown in Fig. 4(a), the feasible set Ψ_2 is partially overlapped with the solution

Authorized licensed use limited to: Stevens Institute of Technology. Downloaded on August 18,2020 at 19:27:31 UTC from IEEE Xplore. Restrictions apply.

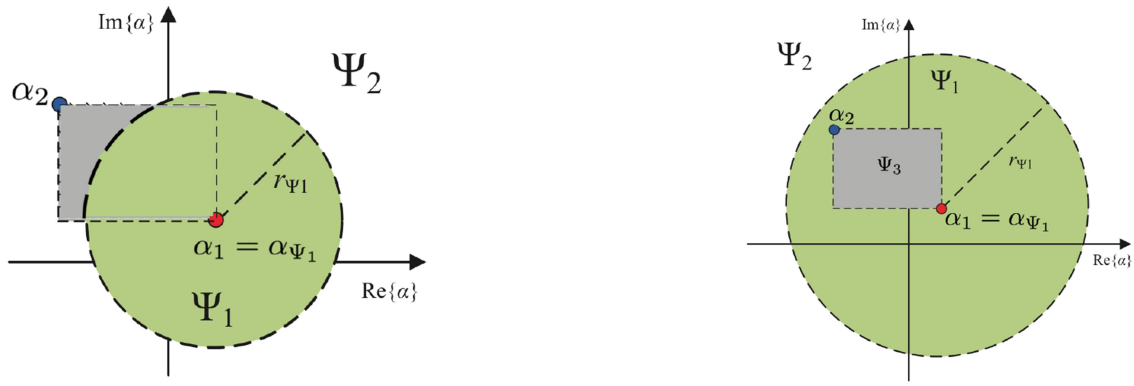

(a) Scenario A: $\Psi_2 \cap \Psi_3 \neq \emptyset$ (b) Scenario B: $\Psi_2 \cap \Psi_3 = \emptyset$

Fig. 4. The geometry for Case III; (a) Scenario A: $\Psi_2 \cap \Psi_3 \neq \emptyset$; and (b) Scenario B: $\Psi_2 \cap \Psi_3 = \emptyset$.

set Ψ_3 to the unconstrained $g_2(\alpha)$. As a result, the solution to the constrained optimization $g_2(\alpha)$ must happen to the *overlapping* area between Ψ_2 and Ψ_3, the grey region in Fig 4(a). Denoted by $\alpha^\sharp$, the optimal solution can be numerically found by a gradient descent method over the grey region. On the other hand, the solution to the constrained optimization of $g_1(\alpha)$ over Ψ_1, denoted as $\alpha^\star$, can be derived by a Lagrangian method, given in Appendix A. Therefore, the global optimized solution in Case III.A is given by

$$\hat{\alpha}_{\text{ML,III-A}} = \begin{cases} \alpha^\sharp, & \text{if } g_1(\alpha^\star) > g_2(\alpha^\sharp) \\ \alpha^\star, & \text{if } g_1(\alpha^\star) \leq g_2(\alpha^\sharp) \end{cases}. \tag{58}$$

The sufficient condition of Scenario A is given by

$$0 < r_{\Psi_1} \leq |\alpha_1 - \alpha_2|^2, \tag{59}$$

where r_{Ψ_1}, α_1 and α_2 are defined in (47), (46) and (52), respectively.

- Scenarios B ($\Psi_2 \cap \Psi_3 = \emptyset$): As shown in Fig. 4(b), the feasible set Ψ_2 has no overlapping with the solution set Ψ_3. Given that $g_2(\alpha)$ is a monotonically increasing function, the fact that the feasible set Ψ_2 excludes Ψ_3 implies that the optimal solution must be located at the boundary of the feasible set Ψ_2. As a result, the constrained optimization $g_2(\alpha)$ over Ψ_2 reduces to

$$\min_{\alpha} g_2(\alpha), \quad \text{s.t.} \left\|\mathbf{P}_{\tilde{\mathbf{H}}}(\mathbf{y} - \alpha\tilde{\mathbf{s}})\right\|^2 = 1, \tag{60}$$

where the equality constraint denotes the circle lower bounded Ψ_2. With the equality constraint, $g_2(\alpha)$ can be rewritten as

$$\begin{aligned} g_2(\alpha) &= (\mathbf{y} - \alpha\tilde{\mathbf{s}})^H \mathbf{P}_{\tilde{\mathbf{H}}}(\mathbf{y} - \alpha\tilde{\mathbf{s}}) \\ &\quad + (\mathbf{y} - \alpha\tilde{\mathbf{s}})^H \mathbf{P}^{\perp}_{\tilde{\mathbf{H}}}(\mathbf{y} - \alpha\tilde{\mathbf{s}}) \\ &= \|\mathbf{y} - \alpha\tilde{\mathbf{s}}\|^2 = g_1(\alpha). \end{aligned} \tag{61}$$

Therefore, (60) reduces to

$$\min_{\alpha} g_1(\alpha), \quad \text{s.t.} \quad \eta(\alpha) = \left\|\mathbf{P}_{\tilde{\mathbf{H}}}(\mathbf{y} - \alpha\tilde{\mathbf{s}})\right\|^2 = 1. \tag{62}$$

Now it is clear to see the the constrained minimization of $g_2(\alpha)$ over Ψ_2 is a special case of constrained minimization of $g_1(\alpha)$ over Ψ_1. Therefore, the global cost function $g(\alpha)$ reduces to

$$\min_{\alpha} g_1(\alpha), \quad \text{s.t.} \quad \eta(\alpha) = \left\|\mathbf{P}_{\tilde{\mathbf{H}}}(\mathbf{y} - \alpha\tilde{\mathbf{s}})\right\|^2 \leq 1, \tag{63}$$

which is minimized at

$$\hat{\alpha}_{\text{ML,III-B}} = \alpha^\star. \tag{64}$$

See Appendix A for the details.
The sufficient condition for this case is given as

$$|\alpha_1 - \alpha_2|^2 < r_{\Psi_1} < \infty, \tag{65}$$

where r_{Ψ_1}, α_1 and α_2 are defined in (47), (46) and (52), respectively.

In a short summary, the local ML estimate of amplitude can be numerically found in **Case I** and **Case III. A** by optimizing a monotonically increasing function over a confined area in the complex-valued domain with explicitly computed initial values and directly solved in closed-form expression in **Case II** and **Case III. B**. The existence conditions for various cases can be explicitly determined with r_{Ψ_1}, α_1 and α_2 defined in (47), (46) and (52), respectively.

D. Test Statistic of Local GLRTs

Given the ML estimates under H_1 and the likelihood functions under both hypotheses, it is straightforward to show that the local GLRT test statistic of (22) is given as follows

$$T(\mathbf{y}) = \begin{cases} \mathbf{y}^H\mathbf{y} - \left\|\mathbf{y} - \hat{\alpha}_{\text{ML}}\tilde{\mathbf{s}}\right\|^2 & \text{if } \eta(\hat{\alpha}_{\text{ML}}) \leq 1, \\ \mathbf{y}^H\mathbf{y} - \ln\left\|\mathbf{P}_{\tilde{\mathbf{H}}}(\mathbf{y} - \hat{\alpha}_{\text{ML}}\tilde{\mathbf{s}})\right\|^2 & \\ -1 - \left\|\mathbf{P}^{\perp}_{\tilde{\mathbf{H}}}(\mathbf{y} - \hat{\alpha}_{\text{ML}}\tilde{\mathbf{s}})\right\|^2 & \text{if } \eta(\hat{\alpha}_{\text{ML}}) > 1 \end{cases} \tag{66}$$

where $\mathbf{y} = \mathbf{R}^{-1/2}\mathbf{x}$ is the whitened received signal, $\mathbf{P}_{\tilde{\mathbf{H}}} = \tilde{\mathbf{H}}(\tilde{\mathbf{H}}^H\tilde{\mathbf{H}})^{-1}\tilde{\mathbf{H}}^H$ and $\mathbf{P}^{\perp}_{\tilde{\mathbf{H}}} = \mathbf{I} - \mathbf{P}_{\tilde{\mathbf{H}}}$ with $\tilde{\mathbf{H}} = \mathbf{R}^{-1/2}\mathbf{H}$ denoting the whitened target residual steering matrix, and $\tilde{\mathbf{s}} = \mathbf{R}^{-1/2}\mathbf{x}$ is the whitened target steering vector. In addition, $\eta(\alpha) = \left\|\mathbf{P}_{\tilde{\mathbf{H}}}(\mathbf{y} - \alpha\tilde{\mathbf{s}})\right\|^2$ and $\hat{\alpha}_{\text{ML}}$ is given in Section IV-C.

Authorized licensed use limited to: Stevens Institute of Technology. Downloaded on August 18,2020 at 19:27:31 UTC from IEEE Xplore. Restrictions apply.

If $\mathbf{R}$ is unknown, we can replace $\mathbf{R}$ in the local GLRT by the sample covariance matrix from G target-free training signals $\mathbf{g}(g), g = 1, \ldots, G$

$$\hat{\mathbf{R}} = \sum_{g=1}^{G} \mathbf{g}(g)\mathbf{g}^H(g), \tag{67}$$

and the local GLRT can be equivalently expressed as

$$\begin{aligned}
&\mathbf{x}^H\hat{\mathbf{R}}^{-1}\mathbf{x} - (\mathbf{x} - \hat{\alpha}_{\mathrm{ML}}\mathbf{s})^H\hat{\mathbf{R}}^{-1}(\mathbf{x} - \hat{\alpha}_{\mathrm{ML}}\mathbf{s}), \quad \text{if } \eta(\hat{\alpha}_{\mathrm{ML}}) \le 1,\\
&\mathbf{x}^H\hat{\mathbf{R}}^{-1}\mathbf{x} - \ln\left[(\mathbf{x} - \hat{\alpha}_{\mathrm{ML}}\mathbf{s})^H\hat{\mathbf{P}}_{\mathbf{H}}(\mathbf{x} - \hat{\alpha}_{\mathrm{ML}}\mathbf{s})\right] - 1\\
&- (\mathbf{x} - \hat{\alpha}_{\mathrm{ML}}\mathbf{s})^H\hat{\mathbf{P}}^{\perp}_{\mathbf{H}}(\mathbf{x} - \hat{\alpha}_{\mathrm{ML}}\mathbf{s}), \quad \text{if } \eta(\hat{\alpha}_{\mathrm{ML}}) > 1,
\end{aligned}$$

where $\hat{\mathbf{P}}_{\mathbf{H}} = \hat{\mathbf{R}}^{-1}\mathbf{H}(\mathbf{H}\hat{\mathbf{R}}^{-1}\mathbf{H})^{-1}\mathbf{H}\hat{\mathbf{R}}^{-1}$ and $\hat{\mathbf{P}}^{\perp}_{\mathbf{H}} = \hat{\mathbf{R}} - \hat{\mathbf{P}}_{\mathbf{H}}$. An interesting observation is that $\eta(\hat{\alpha}_{\mathrm{ML}})$ can be considered as an estimate of the significance of the target residual. If $\eta(\hat{\alpha}_{\mathrm{ML}}) \le 1$, the local GLRT reduces to the conventional AMF which essentially ignores the presence of the target residual. Otherwise (if $\eta(\hat{\alpha}_{\mathrm{ML}}) > 1$), the local GLRT takes into account the target residual in the test statistic.

In [44], we developed an early *ad hoc* solution to the local GLRT. Instead of explicitly solving the ML estimation of the amplitude, it finds an estimate of the amplitude α based on a quantity which cannot be computed from the observations. Then, this quantity is replaced by a *posterior* estimate with the amplitude estimate. Based on the *ad hoc* estimate of α, an approximate GLRT is derived. Albeit simpler, it loses the asymptotic optimality of the true ML estimation and the GLRT. In Section V-A, we compare the proposed exact GLRT with the *ad hoc* GLRT of [44] and show the improved performance of the true local GLRT proposed in this section.

E. Distributed MIMO-GLRT

According to (22), the MIMO-GLRT detector non-coherently combines the local GLRT test statistics as

$$T_{\text{MIMO-MTD}}(\mathbf{Y}) = \sum_{n,i} T(\mathbf{y}_{ni}, \tilde{\mathbf{s}}_{ni}, \tilde{\mathbf{H}}_{ni}), \tag{68}$$

where $\mathbf{Y} = [\mathbf{y}_{11}, \ldots, \mathbf{y}_{1M}, \mathbf{y}_{21}, \ldots, \mathbf{y}_{NM}]$ with $\mathbf{y}_{ni} = \mathbf{R}_{ni}^{-1/2}\mathbf{x}_{ni}$ in the case of a known $\mathbf{R}$ or $\mathbf{y}_{ni} = \hat{\mathbf{R}}_{ni}^{-1/2}\mathbf{x}_{ni}$ if $\mathbf{R}_{ni}$ is unknown

$$\hat{\mathbf{R}}_{ni} = \sum_{g=1}^{G} \mathbf{g}_{ni}(g)\mathbf{g}_{ni}^H(g). \tag{69}$$

with $\mathbf{g}_{ni}(g)$ denoting the g-th training signal for the (n,i)-th Tx-Rx pair. Furthermore, $\tilde{\mathbf{s}}_{ni} = \mathbf{R}_{ni}^{-1/2}\mathbf{s}_{ni}$ and $\hat{\alpha}_{ni,\mathrm{ML}}$ are given by the exact ML solution in Section IV-C. It is worth noting that the final decision is made by aggregating the local test statistics to a central unit.

F. Cramér-Rao Bound for Amplitude Estimation

It is seen that the main step of deriving the GLRT statistic is to derive closed-form ML estimation of the residual subspace covariance matrix $\mathbf{\Sigma}$ and the amplitude α. Therefore, it is worth examining the ML estimation performance and comparing it with corresponding CRB. As detailed in Appendix B, the FIM for estimating α and $\mathbf{\Sigma}$ is decoupled and shows a diagonal block structure; see Eq. (90). Thanks to the diagonal block structure, the diagonal FIM block $\mathbf{I}_{\boldsymbol{\theta}_t\boldsymbol{\theta}_t}$ for estimating the real and imaginary parts of amplitude $\boldsymbol{\theta}_t = [\Re\{\alpha\}, \Im\{\alpha\}]$ can be computed as

$$\mathbf{I}_{\boldsymbol{\theta}_t\boldsymbol{\theta}_t} = 2\Re\left\{\mathbf{s}^H(\mathbf{H}\mathbf{\Sigma}\mathbf{H}^H + \mathbf{R})^{-1}\mathbf{s}\right\}\mathbf{I}_2. \tag{70}$$

By taking the inverse of the FIM block, the CRB for the amplitude estimation is given as

$$\mathrm{CRB}(\alpha) = \frac{1}{\mathbf{s}^H(\mathbf{H}\mathbf{\Sigma}\mathbf{H}^H + \mathbf{R})^{-1}\mathbf{s}}. \tag{71}$$

Similarly, the CRB for estimating the residual subspace covariance matrix $\mathbf{\Sigma}$ can be found by taking the inverse of the FIM block $\mathbf{I}_{\boldsymbol{\theta}_s\boldsymbol{\theta}_s}$ of (92) where $\boldsymbol{\theta}_s = [\mathrm{diag}\{\mathbf{\Sigma}_u\}, \mathrm{vec}\{\Re(\mathbf{\Sigma}_{\mathrm{u}})\}, \mathrm{vec}\{\Im(\mathbf{\Sigma}_{\mathrm{u}})\}]$ groups all real parameters in $\mathbf{\Sigma}$ with $\mathbf{X}_u$ denoting the upper triangular matrix of $\mathbf{X}$ and $\mathrm{diag}\{\mathbf{X}\}$ denoting the diagonal elements of $\mathbf{X}$.

V. Simulation

In this section, simulation results are provided to demonstrate the performance of the proposed MIMO-GLRT detector. We compare the proposed exact MIMO-GLRT with 1) the clairvoyant matched filter (denoted as **MF1**) which is aware of the target residual and also has perfect knowledge of the residual covariance matrix $\mathbf{\Sigma}_{ni}$ and the disturbance covariance matrix $\mathbf{R}_{ni}$, 2) matched filter (denoted as **MF2**) that ignores the target residual but assumes the knowledge of $\mathbf{R}_{ni}$, and 3) the *ad hoc* GLRT proposed in [44]. For the local GLRT, we also include the PMF.

A. Detection Performance of Local GLRT

In the case of $M = 1$ and $N = 1$, i.e., mono-static transceivers, the distributed MIMO-GLRT reduces to the local GLRT. To evaluate the detection performance, we consider the same example used in [44]. Specifically, we have $K = 16$ and the steering vector $\mathbf{s}$ is given by the Fourier basis vector $\mathbf{u}(f) = [1, e^{-j2\pi f}, \ldots, e^{-j2\pi(K-1)f}]^T/\sqrt{K}$ with $f = 3.8/K$, i.e., $\mathbf{s} = \mathbf{u}(3.8/K)$. The signal-to-noise ratio (SNR) is defined as

$$\mathrm{SNR} = |\alpha|^2\mathbf{s}^H\mathbf{R}^{-1}\mathbf{s}, \tag{72}$$

where the noise covariance matrix $\mathbf{R}$ is chosen as $[\mathbf{R}]_{\ell\kappa} = \rho^{|\ell-\kappa|}$ with $\rho = 0.9$ [44]. The target residual with $r = 3$ is generated by using $\mathbf{H} = [\mathbf{u}(f_1), \mathbf{u}(f_2), \mathbf{u}(f_3)]$ with $\{f_i\}_{i=1}^3 = [1/K, 2/K, 3/K]$ and the covariance matrix $\mathbf{\Sigma}$ is chosen as $[\mathbf{\Sigma}]_{\ell\kappa} = \gamma\rho^{|\ell-\kappa|}$ with $\rho = 0.6$, where γ is properly chosen to meet the preset covariance mismatch ratio

$$\epsilon = \frac{\mathrm{tr}\{\mathbf{H}\mathbf{\Sigma}\mathbf{H}^H\} + \mathrm{tr}\{\mathbf{R}\}}{\mathrm{tr}\{\mathbf{R}\}} = \frac{\mathrm{tr}\{\mathbf{\Sigma}\}}{\mathrm{tr}\{\mathbf{R}\}} + 1 \ge 1. \tag{73}$$

The performance is evaluated in terms of the ROC by using Monte-Carlo trials.

Fig. 5 shows the ROC performance of the proposed detector with four mismatch ratios. First, the results confirm that, by

Authorized licensed use limited to: Stevens Institute of Technology. Downloaded on August 18,2020 at 19:27:31 UTC from IEEE Xplore. Restrictions apply.

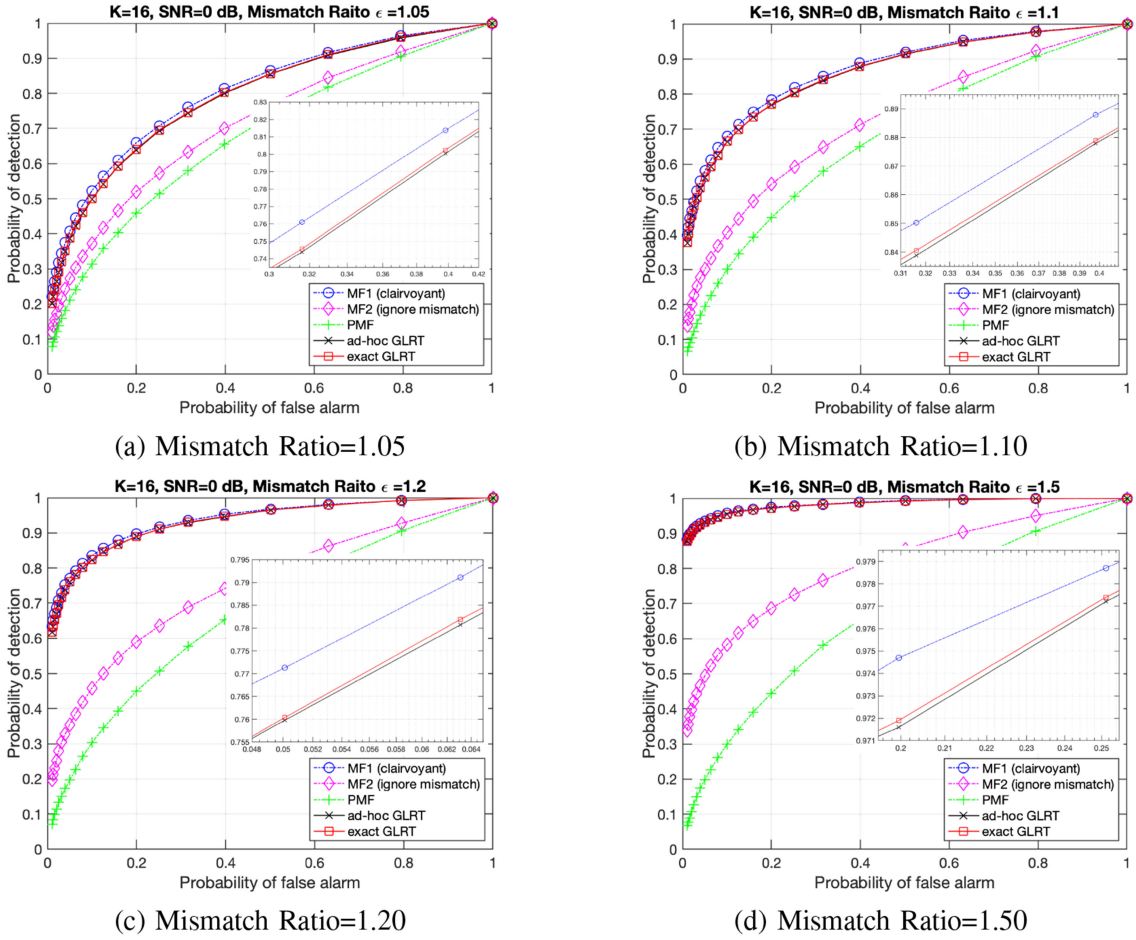

(a) Mismatch Ratio=1.05 (b) Mismatch Ratio=1.10

(c) Mismatch Ratio=1.20 (d) Mismatch Ratio=1.50

Fig. 5. ROC (receiver operating characteristic) curves for various local detectors as a function of mismatch ratio when SNR = 0 dB. MF1: the optimal matched filter with the knowledge of target residual; MF2: matched filter ignoring the target residual; PMF: projection matched filter; Ad hoc: an *ad hoc* GLRT of [44]; GLRT: proposed GLRT.

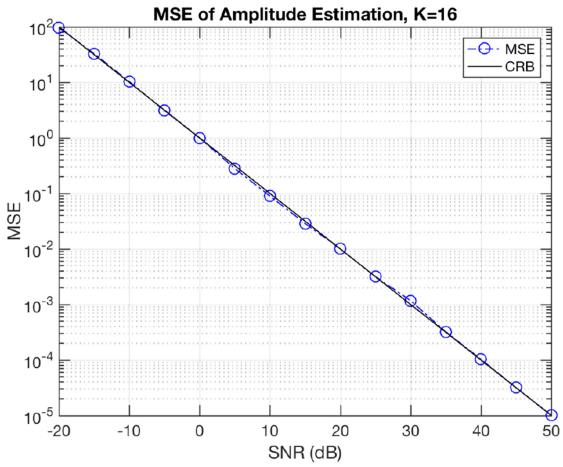

Fig. 6. MSE of the ML estimation of amplitude and corresponding CRB.

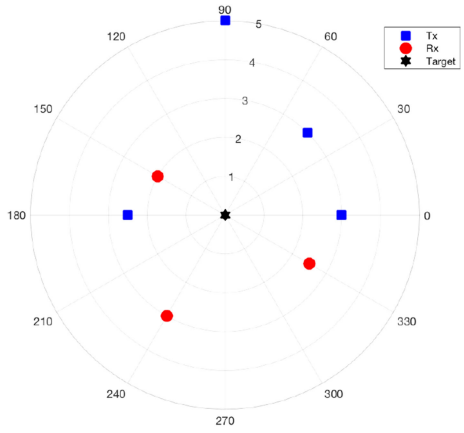

Fig. 7. The distributed MIMO radar configuration considered in simulation.

exploiting the target residual (i.e., MF1, *ad hoc* GLRT and the exact GLRT), the detection performance can be improved. Specifically, the detection performance of the three detectors that acknowledging the target residual is better than that of MF2 which simply ignores the existence of target residual. Second, larger performance improvement can be achieved if the target residual component is stronger (i.e., with larger mismatch ratio). This observation is intuitive as the stronger the target

Authorized licensed use limited to: Stevens Institute of Technology. Downloaded on August 18,2020 at 19:27:31 UTC from IEEE Xplore. Restrictions apply.

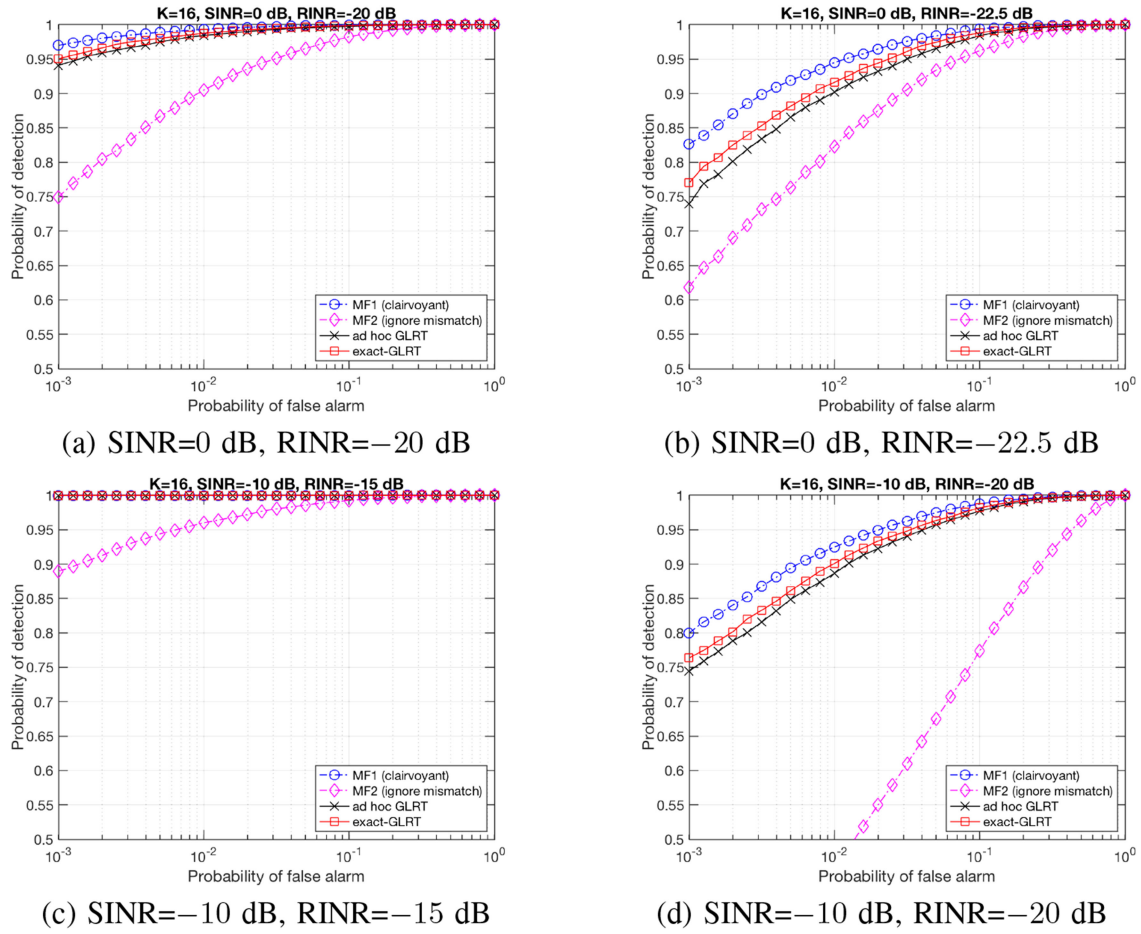

(a) SINR=0 dB, RINR=−20 dB (b) SINR=0 dB, RINR=−22.5 dB

(c) SINR=−10 dB, RINR=−15 dB (d) SINR=−10 dB, RINR=−20 dB

Fig. 8. ROC curves for various distributed MTD detectors as a function of SINR and RINR. First row: SINR $= 0$ dB with RINR $= \{-20, -22.5\}$ dB; Second row: SINR $= -10$ dB with RINR $= \{-15, -20\}$ dB.

residual, the larger the separation between the null and alternative hypotheses and, hence, the better detection performance. Third, the proposed exact local GLRT obtains further performance gain over the *ad hoc* GLRT of [44]. In fact, the exact GLRT almost achieves the performance of the clairvoyant MF1 that requires the perfect knowledge of the residual covariance matrix. Finally, the proposed exact local GLRT provides improved performance than the projection-based PMF by a large margin.

B. ML Estimation of Amplitude

Next, we evaluate the ML estimation of the amplitude in terms of mean-square error (MSE) and compare it with the CRB derived in Section IV-F. As shown in (71), the CRB for amplitude estimation is inversely proportional to the factor $\mathbf{s}^H(\mathbf{H}\boldsymbol{\Sigma}\mathbf{H}^H + \mathbf{R})^{-1}\mathbf{s}$ which is used as the SNR here. We generate the received signal under H_1 as the same as the previous section. Fig. 6 shows the MSE computed from 200 Monte-Carlo runs at each SNR and the corresponding CRB for the amplitude estimation. It is shown that the MSE and CRB linearly decrease in the dB scale. And the simulated MSE matches well with the CRB over all considered SNRs.

C. Detection Performance of Distributed MIMO Radar

Next, we consider a scenario of distributed MIMO configuration. As shown in Fig. 7, the distributed MIMO radar has four transmitters (blue squares) at $\{\theta_{ti}\}_{i=1}^4 = (0^\circ, 45^\circ, 90^\circ, 180^\circ)$ with corresponding distances $(3, 3, 5, 2.5)$ km with respect to the target, and two receivers (red circles) at $\{\theta_{rm}\}_{m=1}^3 = (150^\circ, 270^\circ, 330^\circ)$ with respective distances $(2, 3, 2.5)$ km. Moreover, the pulse repetition frequency (PRF) is 500 Hz, the carrier frequency is 1 GHz, and the number of pulses within a CPI is $K = 16$. The target (dark hexagram) is located in the center with a velocity 108 km/h moving toward 30°. The above parameters lead to a normalized target Doppler frequency given by (5). For a given (ni)-th Tx-Rx pair, the Doppler steering vector $\mathbf{s}(f_{ni})$ is given by the Fourier basis vector $\mathbf{u}(f) = [1, e^{-j2\pi f}, \ldots, e^{-j2\pi(K-1)f}]^T/\sqrt{K}$ with f given by (5), while the target residual matrix $\mathbf{H}_{ni} \in \mathbb{C}^{K\times(M-1)}$ is given as

$$\mathbf{H}_{ni} = [\mathbf{u}(f_{n1}), \ldots, \{\mathbf{u}(f_{nm})\}_{m\neq i}, \ldots, \mathbf{u}(f_{nM})], \qquad (74)$$

where $\{f_{nm}\}_{m\neq i}$ is also computed by (5) but with different $\{\theta_{ti}, \theta_{rn}\}$. In addition, the disturbance (interference-plus-noise)

Authorized licensed use limited to: Stevens Institute of Technology. Downloaded on August 18,2020 at 19:27:31 UTC from IEEE Xplore. Restrictions apply.

covariance matrix $\mathbf{R}_{ni}$ is given as

$$[\mathbf{R}_{ni}]_{\ell\kappa} = \rho_{ni}^{|\ell-\kappa|}, \tag{75}$$

with ρ_{ni} is chosen to be different for different Tx-Rx pairs, and the target residual covariance matrix $\mathbf{\Sigma}_{ni}$ is given as

$$[\mathbf{\Sigma}_{ni}]_{\ell\kappa} = \beta_{ni}^{|\ell-\kappa|}, \tag{76}$$

where β_{ni} is chosen to be different for different Tx-Rx pairs. The average signal-to-interference-plus-noise ratio (SINR) is defined as

$$\text{SINR} = \frac{\sum_{n,i} |\alpha_{ni}|^2 \mathbf{s}(f_{ni})^H \mathbf{R}_{ni}^{-1} \mathbf{s}(f_{ni})}{MN}, \tag{77}$$

and the residual-to-interference-plus-noise ratio (RINR) is defined as

$$\text{RINR} = \sum_{n,i} \frac{\text{tr}\{\mathbf{\Sigma}_{ni}\}}{MN\text{tr}\{\mathbf{R}_{ni}\}}. \tag{78}$$

Fig. 8 shows the ROC performance of the considered distributed MTD detectors with different SINRs and RINRs. Fig. 8(a) and (b) consider a case of SINR $= 0$ dB. Since the target residual may be weak compared with the target signal, we consider a case of RINR $= -20$ dB and RINR $= -22.5$ dB, which is 20 dB weaker than the target signal. In fact, considering $K = 16$ and the high target velocity, the target residual may appear to be even smaller than what may be observed in practice. The results in Fig. 8(a) and (b) confirm that, the larger the target residual, the better the detection performance. At a probability of false alarm at $P_f = 0.001$, the proposed exact GLRT can achieve a probability of detection around $P_d = 95\%$, while the MF2 detector that ignores the target residual yields a performance around $P_d = 77\%$. When the target residual is even weaker, e.g., RINR $= -22.5$ dB, it appears that the exact GLRT detector shows a smaller performance gain over the MF2, while the clairvoyant MF1 still holds a reasonable performance margin over the MF2.

Next, we reduce the SINR to SINR $= -10$ dB. As shown in Fig. 8(d), with the same RINR of RINR $= -20$ dB, the detection performance is reduced compared with the case of SINR $= 0$ dB (comparing red curves in Fig. 8(a) and Fig. 8(d)). Particularly, the detection performance of the MF1 is significantly lower and has a detection performance around $P_d = 20\%$ when $P_f = 0.001$, while the proposed GLRT detector can still achieve a performance around $P_d = 75\%$. By increasing the strength of the target residual to RINR $= -15$ dB in Fig. 8(c), the detection performance (red curves) of the proposed GLRT detector almost reaches the detection performance at $P_d = 100\%$, while the MF2 achieves a detection performance around $P_d = 90\%$ when $P_f = 0.001$.

VI. Conclusion

In this paper, we considered moving target detection using distributed MIMO radars with orthogonal transmitting waveforms. Particularly, we took into account target residual terms in the baseband receiving signal due to imperfect waveform separation and developed explicit subspace signal models for the target residual component at local receivers. Depending on assumptions on the target amplitude over a scan, fluctuating or non-fluctuating, we re-formulated the moving target detection problem into a binary composite hypothesis testing in a distributed subspace framework. We paid attention to the distributed hybrid-order Gaussian model and developed the exact GLRT framework by finding the maximum likelihood estimates of the amplitude and residual covariance subspace. With numerical verification in local and distributed scenarios, we confirmed the effectiveness of the proposed GLRT and showed performance gain in terms of ROC by exploiting the existence of target residual component. Future works may include analytical performance analysis of the proposed detector (e.g., probability of false alarm and probability of detection) and performance validation with more realistic datasets.

Appendix

A. Solution to (63)

First, we rewrite (63) as

$$\min_{\alpha} \|\mathbf{y} - \alpha\tilde{\mathbf{s}}\|^2, \text{s.t. } \|\mathbf{P}_{\tilde{\mathbf{H}}}(\mathbf{y} - \alpha\tilde{\mathbf{s}})\|^2 \leq 1. \tag{79}$$

And note that $g_1(\alpha) = \|\mathbf{y} - \alpha\tilde{\mathbf{s}}\|^2$ is optimized at

$$\alpha_3 = \frac{\tilde{\mathbf{s}}^H \mathbf{y}}{\tilde{\mathbf{s}}^H \tilde{\mathbf{s}}}. \tag{80}$$

On the other hand, the constraint set is given by Ψ_1, i.e., $\|\mathbf{P}_{\tilde{\mathbf{H}}}(\mathbf{y} - \alpha\tilde{\mathbf{s}})\|^2 \leq 1$ which is centered at α_1. It is easy to see that both the cost function and constraint are quadratic function over α. The equivalent unconstrained optimization problem via the Lagrange multiplier method is to minimize the expanded function over α and λ

$$\mathcal{L}(\alpha, \lambda) = \|\mathbf{y} - \alpha\tilde{\mathbf{s}}\|^2 + \lambda(\|\mathbf{P}_{\tilde{\mathbf{H}}}(\mathbf{y} - \alpha\tilde{\mathbf{s}})\|^2 - 1). \tag{81}$$

Taking the derivative of $\mathcal{L}(\alpha, \lambda)$ over α gives

$$\alpha = (1 - \theta)\alpha_1 + \theta\alpha_3, \tag{82}$$

where α_3 is given in (80),

$$\alpha_1 = \frac{\mathbf{s}^H \mathbf{P}_{\tilde{\mathbf{H}}} \mathbf{y}}{\mathbf{s}^H \mathbf{P}_{\tilde{\mathbf{H}}} \mathbf{s}}, \tag{83}$$

given in (46), and the weight θ is a function of non-negative λ

$$\theta = \frac{\lambda(\tilde{\mathbf{s}}^H \mathbf{P}_{\tilde{\mathbf{H}}} \mathbf{s})}{\tilde{\mathbf{s}}^H \tilde{\mathbf{s}} + \lambda \tilde{\mathbf{s}}^H \mathbf{P}_{\tilde{\mathbf{H}}} \mathbf{s}}. \tag{84}$$

It is noted that $0 \leq \theta \leq 1$ which implies that α is a convex combination of α_1 and α_3 and is located in between these two points in the complex-valued domain.

Taking the derivative of (α, λ) over λ, we have

$$\|\mathbf{P}_{\tilde{\mathbf{H}}}(\mathbf{y} - \alpha\tilde{\mathbf{s}})\|^2 = 1, \tag{85}$$

which can be rewritten as $e|\alpha - \alpha_1|^2 + a/e = 1$, where a and e are defined, respectively, in (48) and (49). Plugging (82) into the above equation and considering $\theta \in [0, 1]$, we have

$$\theta^* = \min\left\{\frac{\frac{\sqrt{e-a}}{e}}{|\alpha_1 - \alpha_3|}, 1\right\} = \min\left\{\frac{r_{\Psi_1}}{|\alpha_1 - \alpha_3|}, 1\right\}. \tag{86}$$

Authorized licensed use limited to: Stevens Institute of Technology. Downloaded on August 18,2020 at 19:27:31 UTC from IEEE Xplore. Restrictions apply.

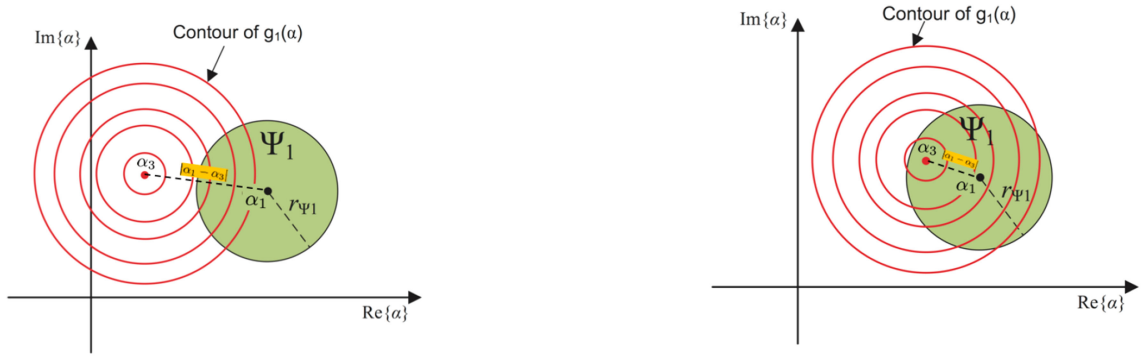

(a) $r_{\Psi_1} \le |\alpha_1 - \alpha_3|$ (b) $r_{\Psi_1} > |\alpha_1 - \alpha_3|$

Fig. 9. The geometry interpretation of α^*.

As a result, we can find a closed-form expression for α as

$$\alpha^* = (1-\theta^*)\alpha_1 + \theta^*\alpha_3. \tag{87}$$

Geometry Interpretation of α^*: It is interesting to interpret the solution α^* in a geometric standpoint; see Fig. 9. First, if $r_{\Psi_1} \le |\alpha_1 - \alpha_3|$, as shown in Fig. 9(a), it implies that the global minimizer to $\|\mathbf{y} - \alpha\tilde{\mathbf{s}}\|^2$, i.e., α_3, is excluded from the feasible set which is a disk centered at α_1 with a radius of r_{Ψ_1}. Since the cost function is a quadratic function over α, the optimal solution in this case must lie on the boundary of the feasible set. More precisely, it is located at the intersection between the line connecting α_1 and α_3 and the boundary of the feasible set. This can be easily determined as

$$\alpha^* = \frac{r_{\Psi_1}}{|\alpha_1 - \alpha_3|}\alpha_1 + \frac{|\alpha_1 - \alpha_3| - r_{\Psi_1}}{|\alpha_1 - \alpha_3|}\alpha_3, \tag{88}$$

which coincides with (87) when $r_{\Psi_1} \le |\alpha_1 - \alpha_3|$.

On the other hand, if $r_{\Psi_1} > |\alpha_1 - \alpha_3|$, the case of Fig. 9(b), the global minimizer to $\|\mathbf{y} - \alpha\tilde{\mathbf{s}}\|^2$, i.e., α_3, is within the feasible set which is a disk centered at α_1 with a radius of r_{Ψ_1}. As a result,

$$\alpha^* = \alpha_3, \tag{89}$$

which also reduces to (87) when $r_{\Psi_1} > |\alpha_1 - \alpha_3|$.

B. FIM of Unknown Parameter Estimation Under H_1

First, group unknown parameters under H_1 as

$$\boldsymbol{\theta} = [\Re\{\alpha\}, \Im\{\alpha\}, \mathrm{diag}\{\boldsymbol{\Sigma}_u\}, \mathrm{vec}\{\Re(\boldsymbol{\Sigma}_{\mathrm{u}})\}, \mathrm{vec}\{\Im(\boldsymbol{\Sigma}_{\mathrm{u}})\}]$$

with $\boldsymbol{\Sigma}_u$ denoting the upper triangular matrix of $\boldsymbol{\Sigma}$ and $\mathrm{diag}\{\mathbf{X}\}$ denoting the diagonal elements of $\mathbf{X}$. Overall, we have $(2+r^2)$ real unknown parameters in $\boldsymbol{\theta}$.

Next we derive the Fisher information matrix (FIM) of the estimate of $\boldsymbol{\theta}$. Note that $\mathbf{y} \sim \mathcal{CN}(\alpha\tilde{\mathbf{s}}, \mathbf{C})$ where $\mathbf{C} = \tilde{\mathbf{H}}\boldsymbol{\Sigma}\tilde{\mathbf{H}}^H + \mathbf{I}$. It is easy to see that the mean $\alpha\tilde{\mathbf{s}}$ is only related to the target parameter $\boldsymbol{\theta}_t = [\Re\{\alpha\}, \Im\{\alpha\}]^T$ where $\Re\{\cdot\}$ and $\Im\{\cdot\}$ denote the real and imaginary parts, respectively, while the covariance matrix $\mathbf{C} = \tilde{\mathbf{H}}\boldsymbol{\Sigma}\tilde{\mathbf{H}}^H + \mathbf{I}$ is a function of the parameter set corresponding to the subspace covariance matrix $\boldsymbol{\theta}_s = [\mathrm{diag}\{\boldsymbol{\Sigma}_u\}, \mathrm{vec}\{\Re(\boldsymbol{\Sigma}_{\mathrm{u}})\}, \mathrm{vec}\{\Im(\boldsymbol{\Sigma}_{\mathrm{u}})\}]$. As a result, the FIM on estimating $\boldsymbol{\theta} = [\boldsymbol{\theta}_t, \boldsymbol{\theta}_s]$ is block diagonal [47, Section 3.9], i.e.,

$$\mathbf{I}(\boldsymbol{\theta}) = \begin{bmatrix} \mathbf{I}_{\boldsymbol{\theta}_t\boldsymbol{\theta}_t} & \mathbf{0}_{2\times r^2} \\ \mathbf{0}_{r^2\times 2} & \mathbf{I}_{\boldsymbol{\theta}_s\boldsymbol{\theta}_s} \end{bmatrix}, \tag{90}$$

where r^2 is the number of real parameters in $\boldsymbol{\Sigma}$.

The first diagonal FIM block $\mathbf{I}_{\boldsymbol{\theta}_t\boldsymbol{\theta}_t}$ can be computed as

$$\mathbf{I}_{\boldsymbol{\theta}_t\boldsymbol{\theta}_t} = 2\Re\left\{\tilde{\mathbf{s}}^H(\tilde{\mathbf{H}}\boldsymbol{\Sigma}\tilde{\mathbf{H}}^H + \mathbf{I})^{-1}\tilde{\mathbf{s}}\right\}\mathbf{I}_2, \tag{91}$$

where $\mathbf{I}_2$ denotes the identity matrix of dimension 2. For the other diagonal FIM block $\mathbf{I}_{\boldsymbol{\theta}_s\boldsymbol{\theta}_s}$, we have the following general expression [47]

$$[\mathbf{I}_{\boldsymbol{\theta}_s\boldsymbol{\theta}_s}]_{\mu,\nu} = \mathrm{tr}\left\{\mathbf{C}^{-1}\left(\tilde{\mathbf{H}}\frac{\partial\boldsymbol{\Sigma}}{\partial[\boldsymbol{\theta}_s]_\mu}\tilde{\mathbf{H}}^H\right)\mathbf{C}^{-1}\left(\tilde{\mathbf{H}}\frac{\partial\boldsymbol{\Sigma}}{\partial[\boldsymbol{\theta}_s]_\nu}\tilde{\mathbf{H}}^H\right)\right\} \tag{92}$$

where $\{\mu,\nu\} = 1, 2, \ldots, r^2$, and $[\boldsymbol{\theta}_s]_\mu$ denotes the μ-th element of $\boldsymbol{\theta}_s$. Noticing that $\boldsymbol{\Sigma}$ is a Hermitian matrix, i.e., $\boldsymbol{\Sigma} = \boldsymbol{\Sigma}^H$, we have the following intermediate results,

$$\frac{\partial\boldsymbol{\Sigma}}{\partial[\boldsymbol{\Sigma}]_{ii}} = \mathbf{J}_{ii}, \quad \frac{\partial\boldsymbol{\Sigma}}{\partial[\Re(\boldsymbol{\Sigma})]_{ij}} = \mathbf{J}_{ij} + \mathbf{J}_{ji},$$

$$\frac{\partial\boldsymbol{\Sigma}}{\partial[\Im(\boldsymbol{\Sigma})]_{ij}} = \sqrt{-1}\mathbf{J}_{ij} - \sqrt{-1}\mathbf{J}_{ji},$$

where $\mathbf{J}_{ij}$ denotes the single-entry matrix that is 1 at the (i,j)-th element and zero elsewhere. As a result, we have

$$\tilde{\mathbf{H}}\frac{\partial\boldsymbol{\Sigma}}{\partial[\boldsymbol{\Sigma}]_{ii}}\tilde{\mathbf{H}}^H = \tilde{\mathbf{H}}\mathbf{J}_{ii}\tilde{\mathbf{H}}^H = \tilde{\mathbf{h}}_i\tilde{\mathbf{h}}_i^H$$

$$\tilde{\mathbf{H}}\frac{\partial\boldsymbol{\Sigma}}{\partial[\Re(\boldsymbol{\Sigma})]_{ij}}\tilde{\mathbf{H}}^H = \tilde{\mathbf{h}}_i\tilde{\mathbf{h}}_j^H + \tilde{\mathbf{h}}_j\tilde{\mathbf{h}}_i^H$$

$$\tilde{\mathbf{H}}\frac{\partial\boldsymbol{\Sigma}}{\partial[\Im(\boldsymbol{\Sigma})]_{ij}}\tilde{\mathbf{H}}^H = \sqrt{-1}(\tilde{\mathbf{h}}_i\tilde{\mathbf{h}}_j^H - \tilde{\mathbf{h}}_j\tilde{\mathbf{h}}_i^H)$$

where $\tilde{\mathbf{h}}_i$ denotes the i-th column of $\tilde{\mathbf{H}}$. As a result, we have

$$\mathbf{I}_{[\boldsymbol{\Sigma}]_{ii},[\boldsymbol{\Sigma}]_{pp}} = |\tilde{\mathbf{h}}_i^H\mathbf{C}^{-1}\tilde{\mathbf{h}}_p^H|^2$$

$$\mathbf{I}_{[\boldsymbol{\Sigma}]_{ii},[\Re(\boldsymbol{\Sigma})]_{lp}} = 2\Re\left\{(\tilde{\mathbf{h}}_i^H\mathbf{C}^{-1}\tilde{\mathbf{h}}_l^H)(\tilde{\mathbf{h}}_p^H\mathbf{C}^{-1}\tilde{\mathbf{h}}_i^H)\right\}$$

$$\mathbf{I}_{[\boldsymbol{\Sigma}]_{ii},[\Im(\boldsymbol{\Sigma})]_{lp}} = -2\Im\left\{(\tilde{\mathbf{h}}_i^H\mathbf{C}^{-1}\tilde{\mathbf{h}}_l^H)(\tilde{\mathbf{h}}_p^H\mathbf{C}^{-1}\tilde{\mathbf{h}}_i^H)\right\}$$

Authorized licensed use limited to: Stevens Institute of Technology. Downloaded on August 18,2020 at 19:27:31 UTC from IEEE Xplore. Restrictions apply.

$$\mathbf{I}_{[[\Re(\boldsymbol{\Sigma})]_{ij}[\Re(\boldsymbol{\Sigma})]_{lp}} = 2\Re\left\{(\tilde{\mathbf{h}}_i^H\mathbf{C}^{-1}\tilde{\mathbf{h}}_l^H)(\tilde{\mathbf{h}}_p^H\mathbf{C}^{-1}\tilde{\mathbf{h}}_j^H)\right\} + 2\Re\left\{(\tilde{\mathbf{h}}_i^H\mathbf{C}^{-1}\tilde{\mathbf{h}}_p^H)(\tilde{\mathbf{h}}_l^H\mathbf{C}^{-1}\tilde{\mathbf{h}}_j^H)\right\}$$

$$\mathbf{I}_{[[\Re(\boldsymbol{\Sigma})]_{ij}[\Im(\boldsymbol{\Sigma})]_{lp}} = -2\Im\left\{(\tilde{\mathbf{h}}_i^H\mathbf{C}^{-1}\tilde{\mathbf{h}}_l^H)(\tilde{\mathbf{h}}_p^H\mathbf{C}^{-1}\tilde{\mathbf{h}}_j^H)\right\} - 2\Im\left\{(\tilde{\mathbf{h}}_p^H\mathbf{C}^{-1}\tilde{\mathbf{h}}_i^H)(\tilde{\mathbf{h}}_j^H\mathbf{C}^{-1}\tilde{\mathbf{h}}_l^H)\right\}$$

$$\mathbf{I}_{[[\Im(\boldsymbol{\Sigma})]_{ij}[\Im(\boldsymbol{\Sigma})]_{lp}} = 2\Re\left\{(\tilde{\mathbf{h}}_i^H\mathbf{C}^{-1}\tilde{\mathbf{h}}_l^H)(\tilde{\mathbf{h}}_p^H\mathbf{C}^{-1}\tilde{\mathbf{h}}_j^H)\right\} - 2\Re\left\{(\tilde{\mathbf{h}}_p^H\mathbf{C}^{-1}\tilde{\mathbf{h}}_i^H)(\tilde{\mathbf{h}}_j^H\mathbf{C}^{-1}\tilde{\mathbf{h}}_l^H)\right\}$$

which allows us compute the other diagonal FIM block $\mathbf{I}_{\boldsymbol{\theta}_s\boldsymbol{\theta}_s}$.

REFERENCES

[1] E. Fishler, A. M. Haimovich, R. S. Blum, L. J. Cimini, Jr, D. Chizhik, and R. A. Valenzuela, "Spatial diversity in radars – models and detection performance," *IEEE Trans. Signal Process.*, vol. 54, no. 3, pp. 823–838, Mar. 2006.

[2] N. A. Goodman, "Optimum and decentralized detection for multistatic airborne radar," *IEEE Trans. Aerosp. Electron. Syst.*, vol. 43, no. 2, pp. 806–813, Apr. 2007.

[3] A. M. Haimovich, R. S. Blum, and L. J. Cimini, "MIMO radar with widely separated antennas," *IEEE Signal Process. Mag.*, vol. 25, no. 1, pp. 116–129, Jan. 2008.

[4] Q. He, R. S. Blum, H. Godrich, and A. M. Haimovich, "Target velocity estimation and antenna placement for MIMO radar with widely separated antennas," *IEEE J. Sel. Topics Signal Process.*, vol. 4, no. 1, pp. 79–100, Feb. 2010.

[5] Q. He, N. H. Lehmann, R. S. Blum, and A. M. Haimovich, "MIMO radar moving target detection in homogeneous clutter," *IEEE Trans. Aerosp. Electron. Syst.*, vol. 46, no. 3, pp. 1290–1301, Jul. 2010.

[6] P. Wang, H. Li, and B. Himed, "Moving target detection using distributed MIMO radar in clutter with nonhomogeneous power," *IEEE Trans. Signal Process.*, vol. 59, no. 10, pp. 4809–4820, Oct. 2011.

[7] P. Wang, H. Li, and B. Himed, "A parametric moving target detector for distributed MIMO radar in nonhomogeneous environment," *IEEE Trans. Signal Process.*, vol. 61, no. 9, pp. 2282–2294, May 2013.

[8] G. Cui, H. Li, and M. Rangaswamy, "MIMO radar waveform design with constant modulus and similarity constraints," *IEEE Trans. Signal Process.*, vol. 62, no. 2, pp. 343–353, Jan. 2014.

[9] S. Ahmed and M. Alouini, "MIMO radar transmit beampattern design without synthesising the covariance matrix," *IEEE Trans. Signal Process.*, vol. 62, no. 9, pp. 2278–2289, May 2014.

[10] A. Aubry, A. De Maio, and Y. Huang, "MIMO radar beampattern design via PSL/ISL optimization," *IEEE Trans. Signal Process.*, vol. 64, no. 15, pp. 3955–3967, Aug. 2016.

[11] W. Fan, J. Liang, and J. Li, "Constant modulus MIMO radar waveform design with minimum peak sidelobe transmit beampattern," *IEEE Trans. Signal Process.*, vol. 66, no. 16, pp. 4207–4222, Aug. 2018.

[12] X. Yu, G. Cui, J. Yang, L. Kong, and J. Li, "Wideband MIMO radar waveform design," *IEEE Trans. Signal Process.*, vol. 67, no. 13, pp. 3487–3501, Jul. 2019.

[13] X. Yu, G. Cui, L. Kong, J. Li, and G. Gui, "Constrained waveform design for colocated MIMO radar with uncertain steering matrices," *IEEE Trans. Aerosp. Electron. Syst.*, vol. 55, no. 1, pp. 356–370, Feb. 2019.

[14] M. Akcakaya and A. Nehorai, "MIMO radar detection and adaptive design under a phase synchronization mismatch," *IEEE Trans. Signal Process.*, vol. 58, no. 10, pp. 4994–5005, Oct. 2010.

[15] Q. He and R. S. Blum, "Cramer-Rao bound for MIMO radar target localization with phase errors," *IEEE Signal Process. Lett.*, vol. 17, no. 1, pp. 83–86, Jan. 2010.

[16] Y. Yang and R. S. Blum, "Phase synchronization for coherent MIMO radar: Algorithms and their analysis," *IEEE Trans. Signal Process.*, vol. 59, no. 11, pp. 5538–5557, Nov. 2011.

[17] S. Gogineni and A. Nehorai, "Target estimation using sparse modeling for distributed MIMO radar," *IEEE Trans. Signal Process.*, vol. 59, no. 11, pp. 5315–5325, Nov. 2011.

[18] B. Li and A. P. Petropulu, "Distributed MIMO radar based on sparse sensing: Analysis and efficient implementation," *IEEE Trans. Aerosp. Electron. Syst.*, vol. 51, no. 4, pp. 3055–3070, Oct. 2015.

[19] T. Zhang, G. Cui, L. Kong, and X. Yang, "Adaptive Bayesian detection using MIMO radar in spatially heterogeneous clutter," *IEEE Signal Process. Lett.*, vol. 20, no. 6, pp. 547–550, Jun. 2013.

[20] T. R. Qureshi, M. Rangaswamy, and K. L. Bell, "Parametric adaptive matched filter for multistatic MIMO radar," *IEEE Trans. Aerosp. Electron. Syst.*, vol. 54, no. 5, pp. 2202–2219, Oct. 2018.

[21] Y. Yang, H. Su, Q. Hu, S. Zhou, and J. Huang, "Centralized adaptive CFAR detection with registration errors in multistatic radar," *IEEE Trans. Aerosp. Electron. Syst.*, vol. 54, no. 5, pp. 2370–2382, Oct. 2018.

[22] H. Godrich, A. P. Petropulu, and H. V. Poor, "Power allocation strategies for target localization in distributed multiple-radar architectures," *IEEE Trans. Signal Process.*, vol. 59, no. 7, pp. 3226–3240, Jul. 2011.

[23] Y. Yu, S. Sun, R. N. Madan, and A. Petropulu, "Power allocation and waveform design for the compressive sensing based MIMO radar," *IEEE Trans. Aerosp. Electron. Syst.*, vol. 50, no. 2, pp. 898–909, Apr. 2014.

[24] Y. Yang *et al.*, "Fast optimal antenna placement for distributed MIMO radar with surveillance performance," *IEEE Signal Process. Lett.*, vol. 22, no. 11, pp. 1955–1959, Nov. 2015.

[25] T. Aittomaki, S. P. Chepuri, and V. Koivunen, "Dynamic transmit power allocation for distributed MIMO radar target detection," in *Proc. IEEE SAM*, Jul. 2018, pp. 282–286.

[26] J. Liu, J. Han, Z. Zhang, and J. Li, "Bayesian detection for MIMO radar in Gaussian clutter," *IEEE Trans. Signal Process.*, vol. 66, no. 24, pp. 6549–6559, Dec. 2018.

[27] J. Liu, W. Liu, J. Han, B. Tang, Y. Zhao, and H. Yang, "Persymmetric GLRT detection in MIMO radar," *IEEE Trans. Veh. Technol.*, vol. 67, no. 12, pp. 11913–11923, Dec. 2018.

[28] J. Liu, W. Liu, B. Tang, J. Zheng, and S. Xu, "Distributed target detection exploiting persymmetry in Gaussian clutter," *IEEE Trans. Signal Process.*, vol. 67, no. 4, pp. 1022–1033, Feb. 2019.

[29] P. Chen, L. Zheng, X. Wang, H. Li, and L. Wu, "Moving target detection using colocated MIMO radar on multiple distributed moving platforms," *IEEE Trans. Signal Process.*, vol. 65, no. 17, pp. 4670–4683, Sep. 2017.

[30] A. R. Chiriyath, B. Paul, and D. W. Bliss, "Radar-communications convergence: Coexistence, cooperation, and co-design," *IEEE Trans. Cogn. Commun. Netw.*, vol. 3, no. 1, pp. 1–12, Mar. 2017.

[31] L. Zheng, M. Lops, X. Wang, and E. Grossi, "Joint design of overlaid communication systems and pulsed radars," *IEEE Trans. Signal Process.*, vol. 66, no. 1, pp. 139–154, Jan. 2018.

[32] Q. He, Z. Wang, J. Hu, and R. S. Blum, "Performance gains from cooperative MIMO radar and MIMO communication systems," *IEEE Signal Process. Lett.*, vol. 26, no. 1, pp. 194–198, Jan. 2019.

[33] F. Daum and J. Huang, "MIMO radar: Snake oil or good idea?" *IEEE Aerosp. Electron. Syst. Mag.*, vol. 24, no. 5, pp. 8–12, May 2009.

[34] M. Akcakaya and A. Nehorai, "MIMO radar sensitivity analysis for target detection," *IEEE Trans. Signal Process.*, vol. 59, no. 7, pp. 3241–3250, Jul. 2011.

[35] A. Zaimbashi, "Invariant subspace detector in distributed multiple-input multiple output radar: Geometry gain helps improving moving target detection," *IET Radar, Sonar Navigat.*, vol. 10, no. 5, pp. 923–934, 2016.

[36] Y. I. Abramovich and G. J. Frazer, "Bounds on the volume and height distributions for the MIMO radar ambiguity function," *IEEE Signal Process. Lett.*, vol. 15, pp. 505–508, May 2008.

[37] Y. Li, S. A. Vorobyov, and V. Koivunen, "Ambiguity function of the transmit beamspace-based MIMO radar," *IEEE Trans. Signal Process.*, vol. 63, no. 17, pp. 4445–4457, Sep. 2015.

[38] L. L. Scharf and B. Friedlander, "Matched subspace detectors," *IEEE Trans. Signal Process.*, vol. 42, no. 8, pp. 2146–2157, Aug. 1994.

[39] S. Kraut and L. L. Scharf, "The CFAR adaptive subspace detector is a scale-invariant GLRT," *IEEE Trans. Signal Process.*, vol. 47, no. 9, pp. 2538–2541, Sep. 1999.

[40] E. J. Kelly, "An adaptive detection algorithm," *IEEE Trans. Aerosp. Electron. Syst.*, vol. 22, no. 1, pp. 115–127, Mar. 1986.

[41] E. Conte, M. Lops, and G. Ricci, "Asymptotically optimum radar detection in compound Gaussian clutter," *IEEE Trans. Aerosp. Electron. Syst.*, vol. 31, no. 2, pp. 617–625, Apr. 1995.

[42] S. Bose and A. Steinhardt, "A maximal invariant framework for adaptive detection with structured and unstructured covariance matrices," *IEEE Trans. Signal Process.*, vol. 43, no. 9, pp. 2164–2175, Sep. 1995.

[43] Y. Jin and B. Friedlander, "A CFAR adaptive subspace detector for second-order Gaussian signals," *IEEE Trans. Signal Process.*, vol. 53, no. 3, pp. 871–884, Mar. 2005.

Authorized licensed use limited to: Stevens Institute of Technology. Downloaded on August 18,2020 at 19:27:31 UTC from IEEE Xplore. Restrictions apply.

[44] P. Wang, J. Fang, H. Li, and B. Himed, "Detection with target-induced subspace interference," *IEEE Signal Process. Lett.*, vol. 19, no. 7, pp. 403–406, Jul. 2012.
[45] M. I. Skolnik, *Introduction to Radar Systems*, 3rd ed. New York, NY, USA: McGraw-Hill, 2001.
[46] F. C. Robey, D. R. Fuhrmann, E. J. Kelly, and R. Nitzberg, "A CFAR adaptive matched filter detector," *IEEE Trans. Aerosp. Electron. Syst.*, vol. 28, no. 1, pp. 208–216, Jan. 1992.
[47] S. M. Kay, *Fundamentals of Statistical Signal Processing: Detection Theory*. Upper Saddle River, NJ, USA: Prentice-Hall, 1998.

Pu Wang (Senior Member, IEEE) received the Ph.D. degree in electrical engineering from the Stevens Institute of Technology, Hoboken, NJ, USA, in 2011.

He is currently a Principal Research Scientist with Mitsubishi Electric Research Laboratories (MERL), Cambridge, MA, USA, where he was an Intern in the summer of 2010. Before returning to MERL, he was a Research Scientist with the Schlumberger-Doll Research, Cambridge, MA, USA, contributing to developments of next-generation logging-while-drilling Acoustics/NMR products. His current research interests include signal processing, Bayesian inference, statistical learning, and their applications to (mmWave and THz) sensing, wireless communications, networks and automotive applications.

Dr. Wang was selected as a Distinguished Speaker of the Society of Petrophysicists and Well Log Analysts (SPWLA) in 2017 for the work "Dipole Shear Anisotropy Using Logging-While-Drilling Sonic Tools." He was the recipient of the Conrad Schlumberger Award for Technical Depth twice in 2017 and 2015 from the Schlumberger (North America) Reservoir Symposium, the IEEE Jack Neubauer Memorial Award from the IEEE Vehicular Technology Society in 2013, and the Outstanding Paper Award from the IEEE AFICON Conference in 2011. He also received the Outstanding Doctoral Thesis in Electrical Engineering Award in 2011, the Edward Peskin Award in 2011, the Francis T. Boesch Award in 2008, and the Outstanding Research Assistant Award in 2007 from the Stevens Institute of Technology. He is an Associate Editor for the IEEE SIGNAL PROCESSING LETTERS.

Hongbin Li (Fellow, IEEE) received the B.S. and M.S. degrees from the University of Electronic Science and Technology of China, Chengdu, China, in 1991 and 1994, respectively, and the Ph.D. degree from the University of Florida, Gainesville, FL, USA, in 1999, all in electrical engineering.

From July 1996 to May 1999, he was a Research Assistant with the Department of Electrical and Computer Engineering, University of Florida. Since July 1999, he has been with the Department of Electrical and Computer Engineering, Stevens Institute of Technology, Hoboken, NJ, USA, where he became a Professor in 2010. He was a Summer Visiting Faculty Member with the Air Force Research Laboratory in the summers of 2003, 2004, and 2009. His general research interests include statistical signal processing, wireless communications, and radars.

Dr. Li was the recipient of the IEEE Jack Neubauer Memorial Award in 2013 from the IEEE Vehicular Technology Society, Outstanding Paper Award from the IEEE AFICON Conference in 2011, Provost's Award for Research Excellence in 2019, Harvey N. Davis Teaching Award in 2003, and Jess H. Davis Memorial Research Award in 2001 from the Stevens Institute of Technology, and Sigma Xi Graduate Research Award from the University of Florida in 1999. He has been a member of the IEEE SPS Signal Processing Theory and Methods Technical Committee (TC) and the IEEE SPS Sensor Array and Multichannel TC, an Associate Editor for the *Signal Processing* (Elsevier), IEEE TRANSACTIONS ON SIGNAL PROCESSING, IEEE SIGNAL PROCESSING LETTERS, and IEEE TRANSACTIONS ON WIRELESS COMMUNICATIONS, as well as a Guest Editor for the IEEE JOURNAL OF SELECTED TOPICS IN SIGNAL PROCESSING and *EURASIP Journal on Applied Signal Processing*. He has been involved in various conference organization activities, including serving as a General Co-Chair for the 7th IEEE Sensor Array and Multichannel Signal Processing (SAM) Workshop, Hoboken, NJ, USA, June 17-20, 2012. He is a member of Tau Beta Pi and Phi Kappa Phi.

Authorized licensed use limited to: Stevens Institute of Technology. Downloaded on August 18,2020 at 19:27:31 UTC from IEEE Xplore. Restrictions apply.